Finite Wear and Soft Elasto-Hydrodynamic Lubrication: Beyond the Classical Frictional Contact of Soft Solids

Stanisław Stupkiewicz

Abstract Two classes of contact problems are discussed, namely *finite-wear* and *soft-EHL* problems, which go beyond the classical framework of frictional contact problems. The focus is on the finite-deformation effects and on the computational strategies adequate for the modelling of those problems. By finite wear we mean here the class of contact and wear problems in which finite deformations and finite shape changes due to wear are allowed. The soft-EHL regime of hydrodynamic lubrication is encountered in the case of lubricated contact of compliant solids, such as elastomers or soft tissues, when a relatively low hydrodynamic pressure suffices to significantly deform the solid. In each case, the respective continuum formulation is first introduced, followed by the description of the finite-element treatment and by representative numerical examples.

1 Introduction

Contact is usually modelled by considering only two most important interaction modes, i.e. by enforcing the non-penetration condition and by introducing friction forces. The non-penetration condition imposes a unilateral constraint on the relative motion of the contacting bodies in the direction normal to the contact surface, while friction is associated with the relative motion in the tangential direction. Despite the severe complexity of tribological interactions, friction is most frequently modelled by the classical Amonton–Coulomb friction model, which involves only one parameter, the friction coefficient, even if more advanced friction models exist and could, in principle, be applied in relevant situations, provided the model parameters are reliably determined from experiment or from micromechanical considerations.

It seems that continuum formulations of frictional contact problems have already reached a considerable level of maturity, and efficient computational techniques exist for this class of problems (Laursen 2002; Wriggers 2006). In this chapter, we

---

S. Stupkiewicz (✉)
Institute of Fundamental Technological Research, Polish Academy of Sciences,
Pawińskiego 5B, 02–106, Warsaw, Poland
e-mail: sstupkie@ippt.pan.pl

A. Popp and P. Wriggers (eds.), *Contact Modeling for Solids and Particles*,
CISM International Centre for Mechanical Sciences 585,
https://doi.org/10.1007/978-3-319-90155-8_3

discuss two classes of contact problems that go beyond the classical framework discussed above. Specifically, we focus on *wear* and on *elasto-hydrodynamic lubrication (EHL)*, in both cases with full account of *finite deformations*. Clearly, both wear and EHL have already been subject of intense research, but the finite-deformation effects (including finite shape changes in the case of wear problems) are significantly less recognized.

Finite deformations are typical for *soft solids* such as polymers, including rubber-like materials, soft tissues, some biomaterials, and others. Focusing on contact interactions, we shall treat all those materials as hyperelastic solids, thus neglecting their complex constitutive behaviour that may involve viscoelasticity, history-dependent behaviour, multiphysics couplings, etc. This is admissible because contact formulations and their computational treatment are essentially independent of the bulk material response. Hence, the contact techniques developed can be combined with virtually any solid model, hyperelasticity being the simplest one in the finite deformation regime.

The first part of this chapter is concerned with modelling of *finite wear* problems. Wear is a process of material removal from a surface that is subjected to frictional contact interaction. Wear processes are usually slow, and thus noticeable effects result from repeated contacts and accumulation of wear over a long period. By *finite wear* we mean here a general class of wear problems in which finite deformations are allowed as well as finite shape changes due to wear (Lengiewicz and Stupkiewicz 2012). The approach adopted here for the modelling of progressive wear belongs to the class of incremental solution strategies. An overview and discussion of the relevant computational strategies is presented in Sect. 4.5. Note that wear is a very complex process with several very distinct mechanisms. The activity of the individual wear mechanisms heavily depends on the materials, on surface properties of the contact pair, as well as on the actual contact conditions. The related aspects of constitutive modelling of wear are not discussed here, and we adopt the classical Archard wear law (Archard 1953).

The second part of this chapter is concerned with modelling of *soft-EHL* problems. Contact in the EHL regime occurs when the contacting surfaces are fully separated by the fluid and when the hydrodynamic pressure in the lubricant film is sufficiently high to cause significant elastic deflections of one or both contacting bodies. The EHL theory (Dowson and Higginson 1977; Hamrock et al. 2004) is a well developed theory with classical applications such as gears and rolling-contact bearings, which belong to the class of so-called hard-EHL problems. There is, however, a growing interest in the soft-EHL regime in which the pressure is relatively low, but the elastic deflections are significant because one or both contacting bodies are highly compliant. At the same time, the pressure is not high enough to cause significant increase of lubricant viscosity (on the contrary, the piezoviscous effect is crucial in the hard-EHL problems).

The chapter is organized as follows. The standard formulation of the finite-deformation, finite-slip frictional contact problem is briefly described in Sect. 2 as a background for further developments. In Sect. 3, the Archard-type wear law is consistently formulated in the finite-deformation framework. The continuum formulation of the finite-wear problem is then provided in Sect. 4 followed by the discussion of the time-integration schemes and computational strategies for modelling of progressive wear. Selected illustrative numerical examples are reported in Sect. 5.

The second part of the chapter, Sects. 6, 7 and 8, is devoted to the soft-EHL problems at finite deformation. Section 6 introduces the Reynolds equation which is the basic tool for the modelling of the lubricant flow in the thin channel between the contacting surfaces. Formulation of the soft-EHL problem is provided in Sect. 7. In particular, the EHL couplings are discussed, including the non-standard coupling that results from the finite-deformation effects, and the finite-element treatment is commented briefly. Finally, illustrative numerical examples are provided in Sect. 8.

2 Finite-Deformation Frictional Contact Problem

Presented below is the standard formulation of the frictional contact problem at finite deformation and finite slip. The formulation is based on the master–slave approach and on the notion of the closest-point projection. For the details and for a broader overview, see the monographs by Laursen (2002) and Wriggers (2006) and references cited therein.

Consider two hyperelastic bodies $\mathcal{B}^{(i)}$, $i = 1, 2$, that occupy domains $\Omega^{(i)}$ in the reference configuration. The boundary of $\Omega^{(i)}$ is divided into three non-overlapping parts: displacements and tractions are prescribed on $\Gamma_u^{(i)}$ and $\Gamma_t^{(i)}$, respectively, while $\Gamma_c^{(i)}$ is the potential contact surface. Deformation of each body is described by the corresponding deformation mapping $\boldsymbol{\varphi}^{(i)}$,

$$\mathbf{x}^{(i)} = \boldsymbol{\varphi}^{(i)}(\mathbf{X}^{(i)}, t), \tag{1}$$

where $\mathbf{X}^{(i)} \in \Omega^{(i)}$, $\mathbf{x}^{(i)} \in \omega^{(i)}$, and $\omega^{(i)} = \boldsymbol{\varphi}^{(i)}(\Omega^{(i)}, t)$ denotes the current configuration.

One of the contact surfaces, say $\Gamma_c^{(1)}$, is selected as the *slave* surface, and the contact pair is defined by projecting a point $\mathbf{x}^{(1)}$ of the deformed slave surface $\gamma_c^{(1)} = \boldsymbol{\varphi}^{(1)}(\Gamma_c^{(1)}, t)$ onto the deformed *master* surface $\gamma_c^{(2)} = \boldsymbol{\varphi}^{(2)}(\Gamma_c^{(2)}, t)$. The projection point is denoted by $\bar{\mathbf{x}}^{(2)}$. Let us introduce parameterization of the master surface $\gamma_c^{(2)}$ by convective coordinates $\boldsymbol{\xi} = \{\xi^1, \xi^2\}$ so that we have $\bar{\mathbf{x}}^{(2)} = \mathbf{x}^{(2)}(\bar{\boldsymbol{\xi}})$, and $\bar{\boldsymbol{\xi}} = \{\bar{\xi}^1, \bar{\xi}^2\}$ are the coordinates of the projection point.

The basic kinematic contact variables are the normal gap g_N and the sliding velocity $\mathbf{v}_T$ that are defined as follows:

$$g_N = (\mathbf{x}^{(1)} - \bar{\mathbf{x}}^{(2)}) \cdot \mathbf{n}, \qquad \mathbf{v}_T = \dot{\bar{\xi}}^{\alpha} \boldsymbol{\tau}_{\alpha}, \tag{2}$$

where $\mathbf{n} = \mathbf{n}^{(2)}$, the unit outer normal to the master surface, is adopted as the normal of the contact pair, $\boldsymbol{\tau}_\alpha = \partial \mathbf{x}^{(2)}/\partial \xi^\alpha$, $\alpha = 1, 2$, is the tangent basis, and repeated indices are implicitly summed over. Further, the spatial (Cauchy) traction vector $\mathbf{t} = \mathbf{t}^{(2)}$ is adopted as the contact traction that is decomposed into the normal and tangential components t_N and $\mathbf{t}_T$, respectively,

$$\mathbf{t} = t_N \mathbf{n} + \mathbf{t}_T, \qquad t_N = \mathbf{t} \cdot \mathbf{n}, \qquad \mathbf{t}_T = t_{T\alpha} \boldsymbol{\tau}^{\alpha}, \tag{3}$$

where $\mathbf{t}^{(2)} = \boldsymbol{\sigma}^{(2)}\mathbf{n}$, $\boldsymbol{\sigma}^{(2)}$ is the Cauchy stress, and $\boldsymbol{\tau}^{\alpha}$ is the cobasis, such that $\boldsymbol{\tau}^{\alpha} \cdot \boldsymbol{\tau}_{\beta} = \delta^{\alpha}_{\beta}$, where δ^{α}_{β} is the Kronecker delta.

The kinematic variables g_N and $\mathbf{v}_T$ and the contact tractions t_N and $\mathbf{t}_T$ are related by the contact constraints, which can be interpreted as a kind of constitutive equations. Specifically, the normal interaction is governed by the unilateral contact condition,

$$g_N \geq 0, \qquad t_N \leq 0, \qquad g_N t_N = 0, \tag{4}$$

and the tangential interaction is assumed to be governed by the Coulomb friction law,

$$\|\mathbf{t}_T\| + \mu t_N \leq 0, \qquad \|\mathbf{v}_T\| \mathbf{t}_T = \mathbf{v}_T \|\mathbf{t}_T\|, \qquad \|\mathbf{v}_T\| (\|\mathbf{t}_T\| + \mu t_N) = 0. \tag{5}$$

Equilibrium of the two-body system is written in the form of the following virtual work principle,

$$G(\boldsymbol{\varphi}, \delta\boldsymbol{\varphi}) = G_1(\boldsymbol{\varphi}^{(1)}, \delta\boldsymbol{\varphi}^{(1)}) + G_2(\boldsymbol{\varphi}^{(2)}, \delta\boldsymbol{\varphi}^{(2)}) + G_c(\boldsymbol{\varphi}, \delta\boldsymbol{\varphi}) = 0 \qquad \forall\, \delta\boldsymbol{\varphi}, \tag{6}$$

where $\boldsymbol{\varphi} = \{\boldsymbol{\varphi}^{(1)}, \boldsymbol{\varphi}^{(2)}\}$, and the virtual displacements $\delta\boldsymbol{\varphi}^{(i)}$ (test functions) vanish on $\Gamma^{(i)}_u$. Here, G_i is defined individually for each body and denotes the virtual work of internal and external forces, excluding the contact forces, thus

$$G_i(\boldsymbol{\varphi}^{(i)}, \delta\boldsymbol{\varphi}^{(i)}) = \int_{\Omega^{(i)}} \mathbf{P}^{(i)} \cdot \operatorname{Grad} \delta\boldsymbol{\varphi}^{(i)} \mathrm{d}V - \int_{\Gamma^{(i)}_t} \mathbf{T}^{*(i)} \cdot \delta\boldsymbol{\varphi}^{(i)} \mathrm{d}S, \tag{7}$$

where $\mathbf{P}^{(i)}$ is the first Piola–Kirchhoff stress, $\mathbf{T}^{*(i)}$ is the surface traction prescribed on the boundary $\Gamma^{(i)}_t$, and Grad is the gradient operator relative to the reference configuration. The virtual work G_c of the contact forces takes the following form

$$G_c(\boldsymbol{\varphi}, \delta\boldsymbol{\varphi}) = \int_{\Gamma^{(1)}_c} (T_N \delta g_N + T_{T\alpha} \delta\bar{\xi}^{\alpha}) \mathrm{d}S. \tag{8}$$

The contact contribution is here integrated over the undeformed slave surface $\Gamma^{(1)}_c$. The *nominal* contact tractions T_N and $\mathbf{T}_T$ have thus been introduced,

$$T_N = j^{(1)} t_N, \qquad \mathbf{T}_T = j^{(1)} \mathbf{t}_T, \tag{9}$$

such that T_N and $\mathbf{T}_T$ refer to the unit area in the undeformed configuration $\Omega^{(1)}$ of the slave body. Here, $j^{(1)}$ is the area transformation factor of the slave surface so that $\mathrm{d}s^{(1)} = j^{(1)}\mathrm{d}S^{(1)}$.

The virtual work principle (6) constitutes the basis of the finite-element treatment. It must be complemented by a suitable regularization technique in order to enforce the contact conditions (4) and (5). In the examples reported below, the augmented Lagrangian method is used for that purpose (Alart and Curnier 1991; Pietrzak and Curnier 1999), see Lengiewicz et al. (2011) for the details of the respective AD-based formulation and finite-element implementation.

3 Archard-Type Wear Law

3.1 Nominal and Spatial Wear Rate

Wear is a process of removal of material from a solid surface subjected to a contact interaction. In a continuum description, the wear rate is defined as the volume (or mass) removed per unit area and unit time. Once finite deformations of the contacting bodies are allowed, the notions of volume and area must refer to a specific configuration of the body, and hence a nominal and spatial wear rate can be defined.

The *nominal wear rate* $\dot{W}^{(i)}$ refers to the undeformed configuration $\Omega^{(i)}$ and is defined in terms of the respective elementary volume $\mathrm{d}V^{(i)}$ and surface area $\mathrm{d}S^{(i)}$, thus

$$\dot{W}^{(i)}\mathrm{d}t = \frac{\mathrm{d}V^{(i)}}{\mathrm{d}S^{(i)}} = \frac{1}{\varrho_0^{(i)}}\frac{\mathrm{d}m^{(i)}}{\mathrm{d}S^{(i)}}, \tag{10}$$

where $\varrho_0^{(i)}$ is the mass density in the undeformed configuration. Similarly, the *spatial wear rate* $\dot{w}^{(i)}$ refers to the current configuration $\omega^{(i)}$,

$$\dot{w}^{(i)}\mathrm{d}t = \frac{\mathrm{d}v^{(i)}}{\mathrm{d}s^{(i)}} = \frac{1}{\varrho^{(i)}}\frac{\mathrm{d}m^{(i)}}{\mathrm{d}s^{(i)}}, \tag{11}$$

where $\mathrm{d}v^{(i)}$ and $\mathrm{d}s^{(i)}$ are the corresponding elementary volume and surface area, respectively, and $\varrho^{(i)}$ is the mass density in the current configuration. The following transformation rule applies to the two wear rates,

$$j^{(i)}\dot{w}^{(i)} = J^{(i)}\dot{W}^{(i)}, \tag{12}$$

where $j^{(i)} = \mathrm{d}s^{(i)}/\mathrm{d}S^{(i)}$ is the area transformation factor that follows from the Nanson's formula ($\mathbf{n}\mathrm{d}s = J\mathbf{F}^{-T}\mathbf{N}\mathrm{d}S$), and $J^{(i)} = \mathrm{d}v^{(i)}/\mathrm{d}V^{(i)} = \det\mathbf{F}^{(i)}$ is the determinant of the deformation gradient $\mathbf{F}^{(i)} = \partial\mathbf{x}^{(i)}/\partial\mathbf{X}^{(i)}$.

3.2 Archard Wear Law at Finite Deformation

The classical wear law of Archard (1953) is adopted here, however, the framework is general, and other wear laws can equally be used. In the original form of the Archard law, the wear volume is assumed to be proportional to the normal force and sliding distance. In the continuum formulation, this corresponds to the wear rate being proportional to the normal pressure and sliding velocity. Assuming that the Coulomb friction law holds, the normal contact pressure is proportional to the sliding friction stress, hence the Archard law can be equivalently expressed in terms of the latter.

Now, the product of the (spatial) friction stress $\mathbf{t}_T$ and sliding velocity $\mathbf{v}_T$ is recognized as the frictional dissipation rate density, namely

$$\dot{d} = \mathbf{t}_T \cdot \mathbf{v}_T, \qquad \dot{D}^{(i)} = j^{(i)} \dot{d}. \tag{13}$$

Here, $\dot{d}$ is the spatial density of frictional dissipation rate that is referred to the area in the current configuration $\omega^{(i)}$, while $\dot{D}^{(i)}$ is the nominal density that is referred to the area in the undeformed configuration $\Omega^{(i)}$, hence the area transformation factor in Eq. $(13)_2$.

The Archard wear law can now be formulated in terms of the frictional dissipation rate, thus

$$\dot{W}^{(i)} = K^{(i)} \dot{D}^{(i)}, \tag{14}$$

where $K^{(i)}$ is the wear coefficient. In this formulation, wear volume is proportional to the energy dissipated due to friction, which provides an energetic interpretation of the Archard wear law (cf. Mróz and Stupkiewicz 1994; Fouvry et al. 1996; Ramalho and Miranda 2006). This formulation provides also a natural way to generalize the Archard law to the case of more complex friction laws, including anisotropic friction (e.g., Mróz and Stupkiewicz 1994).

Alternatively, proportionality between the spatial quantities can be postulated, thus leading to the Archard wear law in the following form:

$$\dot{w}^{(i)} = k^{(i)} \dot{d}. \tag{15}$$

By applying the transformation rule (12), the corresponding nominal form is the following:

$$\dot{W}^{(i)} = \frac{1}{J^{(i)}} k^{(i)} \dot{D}^{(i)}, \tag{16}$$

which is *not* equivalent to the spatial one (14). In fact, Eqs. (14) and (16) imply the transformation relationship $k^{(i)} = J^{(i)} K^{(i)}$ between the wear coefficients $K^{(i)}$ and $k^{(i)}$, so that if one of them is a constant then the other one is not a constant, as it depends on the deformation in the subsurface layer. The difference between the two forms vanishes when the material is incompressible ($J^{(i)} = 1$) or when the deformation is small.

Considering that the wear coefficients may, in principle, depend on contact variables, e.g., on the contact pressure, sliding velocity, temperature, etc., the choice between the nominal or spatial form of the Archard wear law is merely free. In particular, there is no experimental evidence that would justify the choice of one or the other form. In the following, the nominal form (14) of the Archard wear law is chosen because, in practice, the wear volume would rather be measured in the undeformed configuration. The nominal wear rate can thus be considered a measurable quantity. Secondly, the computational treatment of the spatial form (16) is more involved because the nominal wear rate $\dot{W}^{(i)}$, which is used in the computational framework, as discussed below, depends then not only on the contact quantities, but also on the deformation in the bulk material (through $J^{(i)}$).

Note that, in an alternative approach (Dragon-Louiset 2001; Peigney 2004; Stolz 2007), the wear criterion is formulated in terms of the thermodynamic driving force for the propagation of a damage interface within the contact subsurface layer. In that case, evaluation of the wear criterion also involves the stresses or strains in the bulk material.

Referring to the finite-element treatment based on the master–slave approach discussed in Sect. 2, we note that the nominal wear rate of the slave surface can be directly determined in terms of the nominal friction traction $\mathbf{T}_T$, namely

$$\dot{W}^{(1)} = K^{(1)} \dot{D}^{(1)}, \qquad \dot{D}^{(1)} = j^{(1)} \dot{d} = j^{(1)} t_{T\alpha} \dot{\bar{\xi}}^{\alpha} = T_{T\alpha} \dot{\bar{\xi}}^{\alpha}. \tag{17}$$

The nominal wear rate of the master surface is then given by

$$\dot{W}^{(2)} = \frac{j^{(2)}}{j^{(1)}} K^{(2)} \dot{D}^{(1)} = \frac{j^{(2)}}{j^{(1)}} \dot{W}_{*}^{(2)}, \qquad \dot{W}_{*}^{(2)} = K^{(2)} \dot{D}^{(1)}, \tag{18}$$

where $\dot{W}_{*}^{(2)}\mathrm{d}t$ can be interpreted as the incremental wear volume of the master surface per unit area of the undeformed slave surface. It is recalled that the wear rates $\dot{W}^{(1)}$ and $\dot{W}^{(2)}$ correspond to the contact pair $(\mathbf{x}^{(1)}, \bar{\mathbf{x}}^{(2)})$ that is defined by the closest-point projection at the current time instant, as discussed in Sect. 2.

4 Finite-Wear Problem

4.1 Finite-Wear Kinematics: Three Configurations

In addition to finite deformation, the two contacting bodies $\mathcal{B}^{(i)}$ are now assumed to undergo finite shape changes due to wear at the contact interface. It is thus convenient to introduce three configurations of the body $\mathcal{B}^{(i)}$: the initial configuration $\hat{\Omega}^{(i)}$, the time-dependent undeformed (worn) configuration $\Omega^{(i)}$, and the current (deformed) configuration $\omega^{(i)}$, cf. Fig. 1. The *shape transformation mapping* $\boldsymbol{\Psi}^{(i)}$ is introduced to describe the shape change due to wear, while, as before, the deformation is described

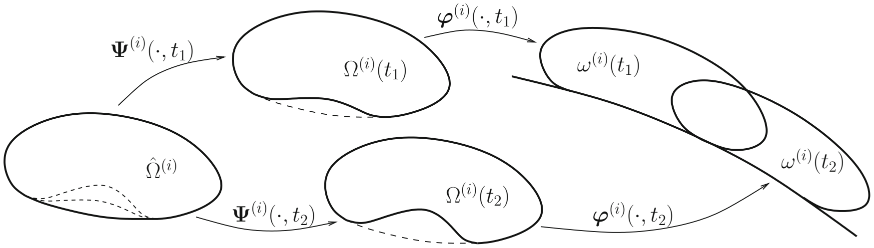

Fig. 1 The three configurations $\hat{\Omega}^{(i)}$, $\Omega^{(i)}$ and $\omega^{(i)}$ at two time instants t_1 and $t_2 > t_1$, shown for one body only (reproduced from Lengiewicz and Stupkiewicz 2012)

by the deformation mapping $\boldsymbol{\varphi}^{(i)}$, thus

$$\mathbf{X}^{(i)} = \boldsymbol{\Psi}^{(i)}(\hat{\mathbf{X}}^{(i)}, t), \qquad \mathbf{x}^{(i)} = \boldsymbol{\varphi}^{(i)}(\mathbf{X}^{(i)}, t), \qquad t \in [0, T], \tag{19}$$

where $\hat{\mathbf{X}}^{(i)} \in \hat{\Omega}^{(i)}$, $\mathbf{X}^{(i)} \in \Omega^{(i)}$ and $\mathbf{x}^{(i)} \in \omega^{(i)}$. For $t > 0$, the initial configuration $\hat{\Omega}^{(i)}$ plays the role of a fixed referential domain for the time-dependent undeformed configuration $\Omega^{(i)}$. If the initial configuration $\hat{\Omega}^{(i)}$ is a stress-free (natural) configuration then the undeformed configuration $\Omega^{(i)}$ is also stress-free.

The finite wear problem at hand comprises two subproblems. The basic unknown in the shape-evolution subproblem is the shape transformation mapping $\boldsymbol{\Psi}^{(i)}$ which is driven by the wear rate. The wear rate results from the deformation subproblem in which the basic unknown is the deformation mapping $\boldsymbol{\varphi}^{(i)}$ that is governed by the equilibrium equation and constitutive relations, along with boundary and contact conditions. As the undeformed configuration $\Omega^{(i)}$, which plays the role of a material reference configuration, evolves in time due to wear, the deformation problem is not a standard one. However, it can be transformed into a standard frictional contact problem, such as that discussed in Sect. 2, by introducing separation of time scales, see Sect. 4.2 below.

As mentioned, the time evolution of the undeformed configuration $\Omega^{(i)}$ results from wear. It is governed by the following relationship, the *shape evolution law*, that links the nominal wear rate $\dot{W}^{(i)}$, see Sect. 3.1, and the time derivative of the shape evolution mapping $\boldsymbol{\Psi}^{(i)}$,

$$\dot{\boldsymbol{\Psi}}^{(i)} \cdot \mathbf{N}^{(i)} = \begin{cases} -\dot{W}^{(i)} & \text{on } \Gamma_c^{(i)}, \\ 0 & \text{on } \partial\Omega^{(i)} \setminus \Gamma_c^{(i)}, \end{cases} \tag{20}$$

where $\partial\Omega^{(i)}$ is the boundary of $\Omega^{(i)}$, $\Gamma_c^{(i)}$ is the potential contact surface, and $\mathbf{N}^{(i)}$ is the unit outer normal in the undeformed configuration $\Omega^{(i)}$. Equation (20) is formulated in the undeformed configuration $\Omega^{(i)}$, i.e., for all $\mathbf{X}^{(i)} \in \partial\Omega^{(i)}$. Accordingly, $\dot{\boldsymbol{\Psi}}^{(i)}$ denotes here $\dot{\boldsymbol{\Psi}}^{(i)} = \dot{\boldsymbol{\Psi}}^{(i)}(\hat{\mathbf{X}}^{(i)}(\mathbf{X}^{(i)}, t), t)$, in view of the one-to-one correspondence between $\mathbf{X}^{(i)}$ and $\hat{\mathbf{X}}^{(i)}$ that is imposed by the shape transformation mapping $\boldsymbol{\Psi}^{(i)}$.

In order to make the notation compact, the above convention is followed below whenever it is convenient and unambiguous.

Note that the shape evolution law (20) prescribes only the normal component of $\dot{\boldsymbol{\Psi}}^{(i)}$ on the boundary $\partial\Omega^{(i)}$. The tangential component is here free, and so is the distribution of $\dot{\boldsymbol{\Psi}}^{(i)}$ in the interior of $\Omega^{(i)}$.

4.2 Separation of Time Scales

The wear process is usually very slow compared to the time scale of the deformation problem. The rate of change of the worn configuration $\Omega^{(i)}$ is thus negligible at this time scale. In other words, the wear rate is negligible compared to the sliding velocity, for instance. It is thus the accumulation of wear over a long time period that leads to a significant change of the worn configuration and to a significant variation of contact conditions.

Let us thus introduce *two time scales*, namely the τ-scale of the deformation problem and the t-scale of the shape changes due to wear. Keeping the shape transformation mapping $\boldsymbol{\Psi}^{(i)}$ unaltered, the deformation mapping $\boldsymbol{\varphi}^{(i)}$ is now expressed in the following form,

$$\mathbf{X}^{(i)} = \boldsymbol{\Psi}^{(i)}(\hat{\mathbf{X}}^{(i)}, t), \quad \mathbf{x}^{(i)} = \boldsymbol{\varphi}_t^{(i)}(\mathbf{X}^{(i)}, \tau), \quad t \in [0, T], \quad \tau \in [t, t + \Delta\tau], \tag{21}$$

where $\mathbf{X}^{(i)} \in \Omega_t^{(i)}$, $\Omega_t^{(i)} = \boldsymbol{\Psi}^{(i)}(\hat{\Omega}^{(i)}, t)$, and $\Delta\tau$ is a characteristic or representative time of the deformation problem, for instance, one cycle of a cyclic loading program. As long as t and τ are varied simultaneously, the deformation mapping $\boldsymbol{\varphi}_t^{(i)}(\mathbf{X}^{(i)}, \tau)$ introduced above is equivalent to that specified by Eq. $(19)_2$.

However, the *separation* of the two time scales can now be assumed such that the deformation problem is analyzed at fixed t and thus for fixed $\Omega_t^{(i)}$. As a result, the deformation problem becomes a standard frictional contact problem, as briefly introduced in Sect. 2, which can be formulated and solved in a standard manner.

Solving the deformation problem at a fixed slow time t yields the deformation mappings $\boldsymbol{\varphi}_t^{(1)}(\mathbf{X}^{(1)}, \tau)$ and $\boldsymbol{\varphi}_t^{(2)}(\mathbf{X}^{(2)}, \tau)$ for $\tau \in [t, t + \Delta\tau]$, and all other quantities involved, such as the contact variables $(t_N, \mathbf{t}_T, \mathbf{v}_T)$. Furthermore, the wear rate $\dot{W}_t^{(i)}(\mathbf{X}^{(i)}, \tau)$ can be computed for all points $\mathbf{X}^{(i)} = \boldsymbol{\Psi}^{(i)}(\hat{X}^{(i)}, t)$ on the potential contact surface $\Gamma_c^{(i)}$ using a suitable wear law, for instance, the Archard law discussed in Sect. 3.2. Computation of the wear rate $\dot{W}_t^{(i)}$ is merely a postprocessing task, as all influential variables are known from the solution of the deformation problem.

The increment $\Delta W_t^{(i)}(\mathbf{X}^{(i)})$ of wear accumulated at $\mathbf{X}^{(i)} \in \Gamma_c^{(i)}$ during the time period $[t, t + \Delta\tau]$ can then be computed by integrating the wear rate $\dot{W}_t^{(i)}$, thus

$$\Delta W_t^{(i)}(\mathbf{X}^{(i)}) = \int_t^{t+\Delta\tau} \dot{W}_t^{(i)}(\mathbf{X}^{(i)}, \tau)\mathrm{d}\tau, \tag{22}$$

and the *average wear rate* at the t-scale, denoted by $\overline{\dot{W}}{}_t^{(i)}(\mathbf{X}^{(i)})$, can be defined as

$$\overline{\dot{W}}{}_t^{(i)}(\mathbf{X}^{(i)}) = \frac{\Delta W_t^{(i)}(\mathbf{X}^{(i)})}{\Delta\tau}. \tag{23}$$

Upon adopting the assumption of separation of time scales, it is the average wear rate $\overline{\dot{W}}{}_t^{(i)}(\mathbf{X}^{(i)})$ that is used in the shape evolution law (20) instead of the instantaneous wear rate $\dot{W}^{(i)}$ in the original finite-wear problem.

In order to apply the assumption of time scale separation, it is required that the shape change associated with the wear increment $\Delta W_t^{(i)}$ accumulated over one deformation cycle is sufficiently small so that its effect on the solution of the deformation problem is negligible. The average wear rate at the t-scale can then be determined as a postprocessing quantity at the τ-scale, and the problem of shape evolution due to wear and the deformation problem are incrementally decoupled. In fact, this decoupling is implicitly assumed in many simulation approaches (e.g., Podra and Andersson 1999; Oqvist 2001; McColl et al. 2004; Hegadekatte et al. 2006; Paulin et al. 2008; Gallego et al. 2010).

Note that, in a general case, specification of the deformation problem at the τ-scale may be nontrivial. In fact, friction is a *path-dependent* phenomenon, and suitable boundary and initial conditions must thus be applied in order to properly describe the complex evolution of stick and slip zones accompanied by the wear-induced shape evolution. In some specific situations, the related problems are easily overcome, for instance, when each loading cycle starts with an open contact (e.g., Paulin et al. 2008; Gallego et al. 2010) or when gross sliding occurs during the loading cycle so that the contact memory is erased.

4.3 Quasi-steady-state Wear Problems

A quasi-steady-state wear problem is defined such that the deformation problem corresponding to a fixed slow time t is a steady-state frictional contact problem once formulated in an appropriate Eulerian frame. Typical examples of quasi-steady-state wear problems are the pin-on-disc tribological test and rolling contact. For instance, in the former case, the reference frame would be attached to the pin, and the disc would be analyzed in an Eulerian frame, or in an arbitrary Lagrangian–Eulerian (ALE) frame in the case of deformable disc.

In a quasi-steady-state wear problem, the deformation subproblem and thus also the deformation mappings $\boldsymbol{\varphi}^{(i)}$ do not depend on the fast time τ, so that we have

$$\mathbf{X}^{(i)} = \boldsymbol{\Psi}^{(i)}(\hat{\mathbf{X}}^{(i)}, t), \qquad \mathbf{x}^{(i)} = \boldsymbol{\varphi}_t^{(i)}(\mathbf{X}^{(i)}), \qquad t \in [0, T], \tag{24}$$

while, as in the general case, the deformation problem is parameterized by the slow time t of the shape evolution problem. The average wear rate at the t-scale is then simply equal to the actual wear rate at the τ-scale, thus

$$\overline{\dot{W}}_t^{(i)}(\mathbf{X}^{(i)}) = \dot{W}_t^{(i)}(\mathbf{X}^{(i)}), \tag{25}$$

and $\dot{W}_t^{(i)}(\mathbf{X}^{(i)})$ does not depend on τ.

In a steady-state frictional contact problem, the motion is decomposed into a background motion which is a rigid-body motion in the undeformed configuration (treated in an Eulerian description) and deformation (treated in a Lagrangian description). This corresponds to a kind of ALE formulation. As the contacting bodies are here assumed hyperelastic, i.e., their behavior is time- and history-independent, and the inertial effects are neglected, the Eulerian rigid-body motion does not affect the deformation problem, except that relative sliding velocity must be properly defined.

The velocity $\mathbf{v}^{(i)}$ of a material point with the position $\mathbf{x}^{(i)}$ in the deformed configuration $\omega^{(i)}$ results solely from the background motion with velocity $\mathbf{V}^{(i)}$ in the undeformed configuration $\Omega^{(i)}$. Specifically, we have

$$\mathbf{v}^{(i)} = \mathbf{F}^{(i)}\mathbf{V}^{(i)}, \tag{26}$$

where $\mathbf{F}^{(i)} = \partial\mathbf{x}^{(i)}/\partial\mathbf{X}^{(i)}$ is the deformation gradient. The sliding velocity $\mathbf{v}_T$ is then defined as the tangential component of the relative velocity,

$$\mathbf{v}_T = v_T^{\alpha}\boldsymbol{\tau}_{\alpha}, \qquad v_T^{\alpha} = (\mathbf{v}^{(1)} - \bar{\mathbf{v}}^{(2)}) \cdot \boldsymbol{\tau}^{\alpha}, \tag{27}$$

where $\boldsymbol{\tau}_{\alpha}$ is the tangent basis, $\boldsymbol{\tau}^{\alpha}$ is the cobasis, and $\bar{\mathbf{v}}^{(2)} = \mathbf{v}^{(2)}(\bar{\mathbf{x}}^{(2)})$ is the velocity of the projection point $\bar{\mathbf{x}}^{(2)}$, see Sect. 2. With this modification, formulation of the steady-state contact problem is identical to that of the general contact problem discussed in Sect. 2.

4.4 Time Integration of Shape Evolution Problem

In order to arrive at a feasible computational scheme, a time integration scheme must be applied to the time-continuous shape evolution problem (20). First-order explicit and implicit Euler schemes are discussed below. A second-order explicit scheme that employs sensitivity analysis in order to arrive at a more accurate approximation of wear increments has been proposed by Lengiewicz and Stupkiewicz (2012).

In the following, two subsequent discrete time instants t_n and $t_{n+1} = t_n + \Delta t$ are thus considered, and a subscript is used to denote the quantities evaluated at a discrete time instant, e.g., $\boldsymbol{\Psi}_{n+1}^{(i)}(\hat{\mathbf{X}}^{(i)}) = \boldsymbol{\Psi}^{(i)}(\hat{\mathbf{X}}^{(i)}, t_{n+1})$. Application of the Euler time integration scheme to the shape evolution law (20) gives

$$\Big(\boldsymbol{\Psi}_{n+1}^{(i)}(\hat{\mathbf{X}}^{(i)}) - \boldsymbol{\Psi}_{n}^{(i)}(\hat{\mathbf{X}}^{(i)})\Big) \cdot \mathbf{N}_{n+\theta}^{(i)}(\hat{\mathbf{X}}^{(i)}) = -\Delta t\, \overline{\dot{W}}_{n+\theta}^{(i)}(\hat{\mathbf{X}}^{(i)}), \tag{28}$$

for $\hat{\mathbf{X}}^{(i)} \in \hat{\Gamma}_c^{(i)}$, while the above condition can be formally extended to the whole boundary $\partial\hat{\Omega}^{(i)}$ by setting $\dot{\overline{W}}{}^{(i)}_{n+\theta}(\hat{\mathbf{X}}^{(i)}) = 0$ for $\hat{\mathbf{X}}^{(i)} \in \partial\hat{\Omega}^{(i)} \setminus \hat{\Gamma}_c^{(i)}$. The explicit forward-Euler scheme and the implicit backward-Euler scheme are obtained for $\theta = 0$ and $\theta = 1$, respectively.

The incremental shape update scheme (28) prescribes only the normal component of the increment of the shape transformation mapping. In order to completely determine $\boldsymbol{\Psi}_{n+1}^{(i)}$ on the boundary, additional assumptions must be adopted concerning its tangential increment on the boundary $\partial\hat{\Omega}^{(i)}$. For instance, one can assume that the shape transformation is such that the points on the contact boundary $\Gamma_c^{(i)}$ are transformed along the normal direction. This yields the following shape update scheme:

$$\boldsymbol{\Psi}_{n+1}^{(i)}(\hat{\mathbf{X}}^{(i)}) = \boldsymbol{\Psi}_{n}^{(i)}(\hat{\mathbf{X}}^{(i)}) - \Delta t\, \dot{\overline{W}}{}^{(i)}_{n+\theta}(\hat{\mathbf{X}}^{(i)})\mathbf{N}_{n+\theta}^{(i)}(\hat{\mathbf{X}}^{(i)}). \tag{29}$$

The time increment Δt in the incremental scheme (28) or (29) is in general independent of the characteristic time $\Delta\tau$ of the deformation problem. In fact, Δt can be adopted much larger than $\Delta\tau$, and its value is actually dictated by the desired accuracy of the time integration scheme and possibly by its stability (see below).

Explicit forward-Euler time integration scheme As already mentioned, the explicit scheme is obtained by setting $\theta = 0$. Eq. (29) can be then be rewritten in the following form

$$\mathbf{X}_{n+1}^{(i)} = \mathbf{X}_{n}^{(i)} - \Delta t\, \dot{\overline{W}}{}^{(i)}_{n}(\mathbf{X}_{n}^{(i)})\mathbf{N}_{n}^{(i)}(\mathbf{X}_{n}^{(i)}), \tag{30}$$

which is the basis of a simple and popular shape update scheme that employs remeshing after the contact problem is solved at each time step (e.g., Podra and Andersson 1999; Oqvist 2001; McColl et al. 2004; Hegadekatte et al. 2006; Paulin et al. 2008). In the context of the finite-element method, the shape update (30) is applied to the boundary nodes. Subsequently, the positions of the interior nodes are determined in a suitable remeshing procedure.

The explicit scheme is simple and easy to implement, but it is only *conditionally stable* so that the time increment must satisfy the stability condition

$$\Delta t < \Delta t_{cr}, \qquad \Delta t_{cr} \sim \frac{h}{E}. \tag{31}$$

As shown by Johansson (1994), the critical time increment Δt_{cr} is proportional to the characteristic mesh size h and inversely proportional to the elastic modulus E. In realistic conditions, the critical time increment may be very small so that the scheme becomes computationally expensive. Conditional stability of the explicit scheme is illustrated by the numerical example reported below.

An approach alternative to the nodal shape update scheme resulting from Eq. (30) has been proposed by Lengiewicz and Stupkiewicz (2012). In that approach, the shape parametrization is independent of the finite-element discretization. Time-dependent shape parameters are introduced for that purpose and the shape evolution law is then enforced approximately through a minimization problem in which evolution of shape parameters is fitted to the wear profile resulting from the finite-element solution of the deformation subproblem. As illustrated by Lengiewicz and Stupkiewicz (2012), independent shape parametrization with a reduced number of shape parameters improves stability of the explicit scheme. To improve accuracy, it can be combined with a second-order explicit scheme that employs shape sensitivity analysis (Stupkiewicz et al. 2010).

Implicit backward-Euler time integration scheme In the case of the fully implicit time integration scheme ($\theta = 1$), the shape update schemes (28) and (29) involve the normal $\mathbf{N}_{n+1}^{(i)}$ and the wear rate $\dot{\overline{W}}_{n+1}^{(i)}$, both evaluated at t_{n+1}. The former explicitly depends on the unknown shape transformation mapping $\boldsymbol{\Psi}_{n+1}^{(i)}$, the latter depends on the unknown solution $\boldsymbol{\varphi}_{n+1}^{(i)}$ of the deformation subproblem at t_{n+1}, and thus it also implicitly depends on $\boldsymbol{\Psi}_{n+1}^{(i)}$. The two subproblems are thus coupled and the problem must be solved simultaneously for $\boldsymbol{\varphi}_{n+1}^{(i)}$ (displacements) and $\boldsymbol{\Psi}_{n+1}^{(i)}$ (shape transformation). Of course, the size of the problem increases due to additional unknowns.

However, the benefit is that the implicit scheme is *unconditionally stable*, so the time increment is limited only by the desired accuracy and not by the stability condition. In practice, significantly larger time increments can be used as compared to the explicit scheme, thus leading to a computationally efficient scheme.

Illustrative example: time integration schemes A numerical example, taken from Stupkiewicz (2013), is provided here to illustrate accuracy and stability of the explicit and implicit time integration schemes and, in particular, the influence of the elastic modulus and finite-element size on the critical time increment, as predicted by Eq. (31).

Consider a hyperelastic (neo-Hookean) pin in plane-strain conditions of the geometry shown in Fig. 2. Its lateral boundaries are constrained in the lateral direction and are free to move in the vertical direction. The pin is pressed into a moving rigid plane by a constant uniform traction that is applied at the top surface. Frictionless contact is considered in this example, and the wear rate is thus assumed to be proportional, with a constant wear coefficient, to the product of contact pressure and sliding velocity. Details concerning geometry and material and process parameters can be found in Stupkiewicz (2013).

The Young's modulus E is varied between 10 and 640 MPa so that, for a fixed prescribed loading, the deformation and the initial contact area are relatively small for $E = 640$ MPa (small deformation regime in Fig. 2) and they are relatively large for $E = 10$ MPa (finite deformation regime, results corresponding to $E = 20$ MPa are shown in Fig. 2).

Wear-induced evolution of the shape of the contact surface is presented in Fig. 3. The shape evolution problem has been integrated using the explicit and the implicit scheme, both with large time increments ($\Delta t = 200$ s, 5 time steps, solid lines) and with small time increments ($\Delta t = 5$ s, 200 time steps, dashed lines). It can be seen that, in the small-deformation regime, the time increment $\Delta t = 200$ s is higher than the critical one for the explicit scheme, and the corresponding results exhibit numerical instability, while the instability is not observed for the smaller time increment

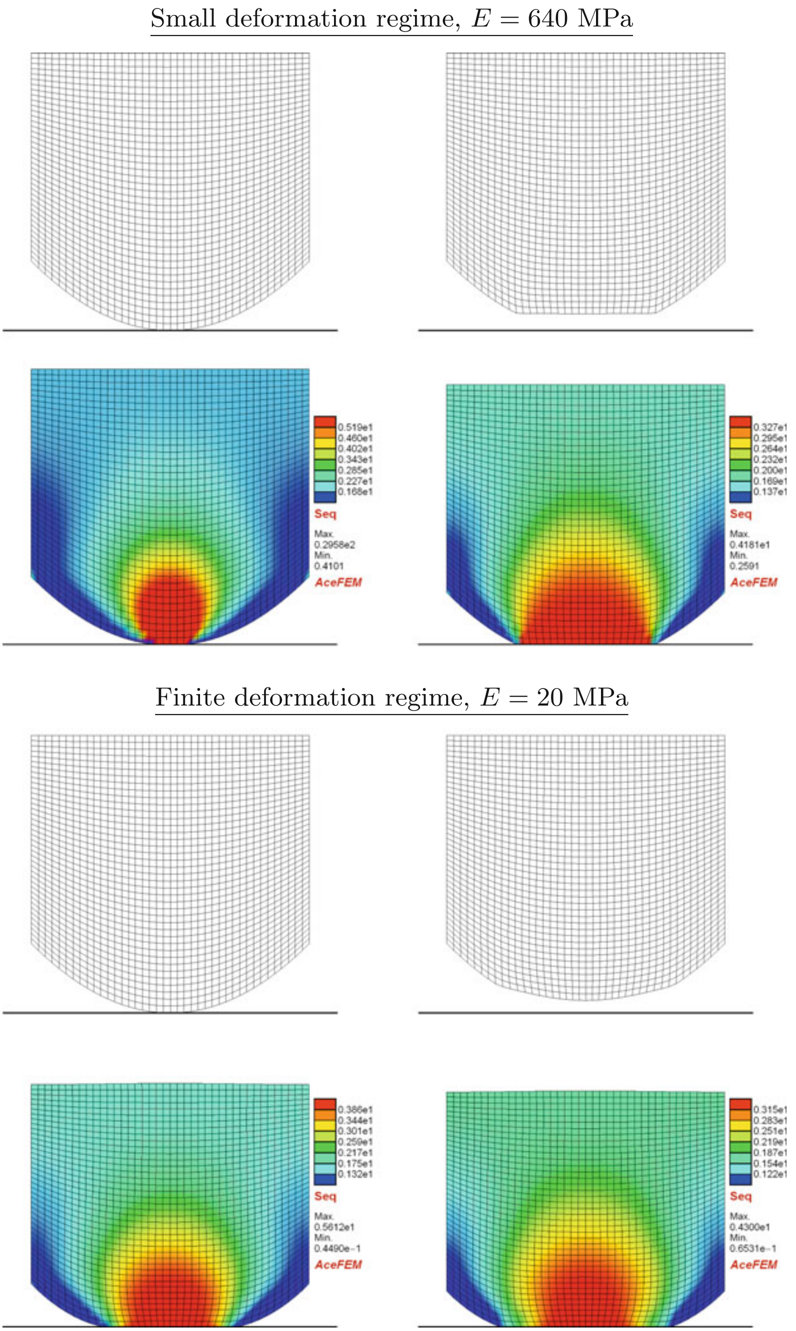

Small deformation regime, $E = 640$ MPa

Finite deformation regime, $E = 20$ MPa

Fig. 2 Two-dimensional pin-on-flat problem in the small-deformation regime (*top*) and in the finite-deformation regime (*bottom*). Finite-element mesh in the undeformed configuration and equivalent stress σ_{eq} in the deformed configuration are shown at the initial time instant $t = 0$ (*left*) and at the final time instant $t = 1000\,\text{s}$ (*right*) (reproduced from Stupkiewicz 2013)

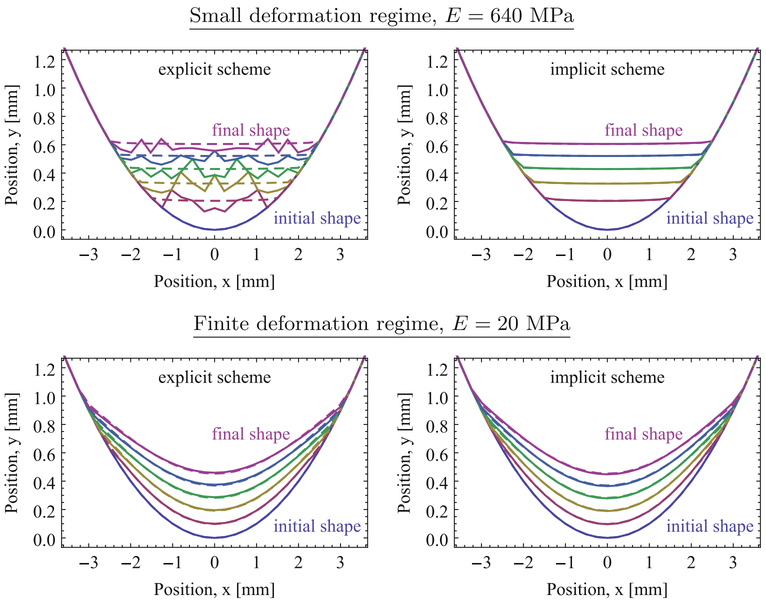

Fig. 3 Two-dimensional pin-on-flat problem: small-deformation (*top*) and finite-deformation (*bottom*) regime. Shape evolution obtained in 5 time steps ($\Delta t = 200$ s, solid lines) and in 200 time steps ($\Delta t = 5$ s, dashed lines) using the explicit (*left*) and implicit (*right*) time integration scheme (reproduced from Stupkiewicz 2013)

$\Delta t = 5$ s. At the same time, the implicit scheme is capable of accurately reproducing significant configuration changes in just 5 time steps. In the finite-deformation regime, the explicit scheme is stable and the accuracy of both schemes is similar. This confirms that the critical time step increases with decreasing elastic modulus, cf. Eq. (31).

A quantitative assessment of accuracy and stability of the two time integration schemes is presented in Fig. 4. The figure shows the solution error as a function of the time increment Δt which has been varied between 1.56 s (640 time steps) and 200 s (5 time steps). Additionally, the Young's modulus E is varied for a fixed mesh density of 80×80 elements, and the mesh density is varied for a fixed Young's modulus $E = 640$ MPa. The solution error has been computed as the Euclidean norm of the difference of the final nodal positions at the contact surface with respect to the reference solution obtained using the time increment of 0.78 s (1280 time steps).

In the case of the implicit scheme, the solution error increases with increasing time increment in an approximately linear manner. This is expected because the Euler scheme is first-order accurate. Similar behavior is observed for the explicit scheme at relatively small time increments. However, a sudden increase of the error is observed at larger time increments. This is related to the instability of the explicit forward-Euler scheme. When the mesh density is increased, for instance, from 20×20 to 40×40 elements so that the element size is decreased by a factor of two, the sudden increase

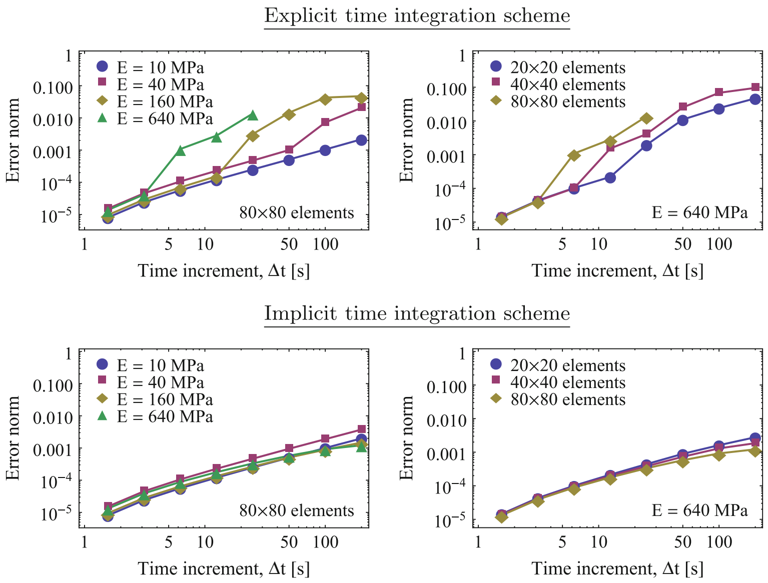

Fig. 4 Two-dimensional pin-on-flat problem: solution error as a function of time increment Δt for the explicit (*top*) and implicit (*bottom*) time integration scheme. Additionally, the elastic modulus E is varied for the mesh of 80×80 elements (*left*) and mesh density is varied for $E = 640$ MPa (*right*) (reproduced from Stupkiewicz 2013)

of the error occurs for a twice smaller time increment. Similar effect is observed when the Young's modulus is varied. Thus, in agreement with the theoretical result of Johansson (1994), see also Eq. (31), the critical time increment is proportional to the element size and inversely proportional to the elastic modulus.

4.5 Shape Update Strategies: Discussion

The incremental solution procedures reported in the literature for the progressive wear problems are usually based on the explicit forward-Euler time integration scheme. This is because computer implementation of the explicit scheme is considerably simpler than implementation of the implicit scheme. The typical explicit procedure amounts to solving the contact problem for the known current shape of the contacting bodies. Knowing the solution of the contact problem, the wear rate can be computed directly as a postprocessing quantity. The wear depth increment is then obtained by multiplying the wear rate by the time increment, the shape is updated accordingly, and the solution proceeds to the next time step. This procedure has been used in combination with the finite-element method (Johansson 1994; Podra and Andersson 1999; Oqvist 2001; McColl et al. 2004; Hegadekatte et al. 2006; Paulin et al. 2008;

Lengiewicz and Stupkiewicz 2012), with the boundary element method (Serre et al. 2001; Sfantos and Aliabadi 2006a; Rodriguez-Tembleque et al. 2012), and with specialized contact solvers (Gallego et al. 2010; Andersson et al. 2011).

When finite configuration changes due to wear are considered, the shape update necessarily involves remeshing (Podra and Andersson 1999; Oqvist 2001; McColl et al. 2004; Hegadekatte et al. 2006; Paulin et al. 2008; Lengiewicz and Stupkiewicz 2012). Alternatively, assuming that the shape changes are small, the shape change can be modelled by simply adding the accumulated wear depth to the initial normal gap (Johansson 1994; Serre et al. 2001; Rodriguez-Tembleque et al. 2012).

As discussed above, the explicit scheme is conditionally stable, and the related instabilities are commonly encountered in computational practice (Johansson 1994; Podra and Andersson 1999; Oqvist 2001; McColl et al. 2004; Sfantos and Aliabadi 2006a; Lengiewicz and Stupkiewicz 2012). The critical time increment decreases with increasing elastic modulus and with decreasing element size, cf. Eq. (31). It follows that mesh refinement increases the computational cost not only due to the increased number of unknowns but also due to the increased number of time steps in view of the stability condition enforced on the time increment. Thus, in problems of practical interest, the solution may be prohibitively expensive.

On the contrary, the implicit backward-Euler scheme is unconditionally stable so that the time increment is constrained only by the desired accuracy of the solution. Application of the implicit scheme requires that the wear increment (or shape transformation resulting from wear) constitutes an additional unknown in the problem. Since the implementation is significantly more involved, the implicit scheme is by far less frequently applied to progressive wear problems (Strömberg 1997; Jourdan and Samida 2009; Ben Dhia and Torkhani 2011; Stupkiewicz 2013; Farah et al. 2017).

In the small-deformation framework adopted by Strömberg (1997), the configuration changes are neglected so that the wear depth could be adopted as an additional unknown to be added to the initial normal gap.

In the approach of Jourdan and Samida (2009), the shape transformation due to wear is restricted to the outer layer of elements only, and the computational treatment is based on the non-smooth contact dynamics method (Jean 1999). The resulting finite-element equations are not fully linearized so that the iterative solution scheme is effectively a modified Newton method. In the implicit scheme developed by Ben Dhia and Torkhani (2011), the coupled wear–deformation problem is not fully linearized either, and the shape transformation is determined using a fixed-point iteration method.

A fully-coupled implicit scheme applicable for quasi-steady-state wear problems has been developed by Stupkiewicz (2013). In this scheme, the shape transformation mapping $\boldsymbol{\Psi}^{(i)}$ and the deformation mapping $\boldsymbol{\varphi}^{(i)}$ constitute the global unknowns of the problem, the former is determined from an auxiliary elasticity problem which is driven by wear increments on the contact boundary. As a result, a kind of an arbitrary Lagrangian–Eulerian (ALE) formulation is obtained in which the shape transformation (i.e., the mesh motion in the finite-element context) is resolved simultaneously with the displacements, all in a fully-implicit monolithic manner. The resulting finite-element equations are solved using the Newton method, and its quadratic convergence is achieved thanks to full linearization of the governing equations.

A general ALE-like scheme has been recently developed by Farah et al. (2017). The incremental scheme is partitioned into a Lagrangian step and a shape evolution step. The Lagrangian step corresponds to the deformation subproblem, and it is performed for a fixed shape of the contacting bodies. However, wear effects within this step are accounted for by adding the accumulated wear increment to the normal gap. In the shape evolution step, the accumulated wear depth is, in a sense, transferred from the normal gap to the new updated mesh. The shape evolution step employs an auxiliary elasticity problem, similar to that used by Stupkiewicz (2013). This partitioned scheme can be iterated until convergence is achieved. The implicit finite wear framework is combined with a state-of-the-art finite-element contact formulation employing dual mortar methods (Popp et al. 2013).

It is worth mentioning that several asymptotic or simplified approaches are available in the literature, which constitute an alternative to the direct incremental schemes discussed above (e.g., Peigney 2004; Paczelt and Mróz 2005; Sfantos and Aliabadi 2006b; Argatov 2011; Lengiewicz and Stupkiewicz 2013; Menga and Ciavarella 2015). These are not discussed here.

5 Finite Wear: Illustrative Examples

Three illustrative examples are provided in this section. The examples are taken from our earlier work (Lengiewicz and Stupkiewicz 2012; Stupkiewicz 2013), where the details can be found along with an extended discussion of the results.

5.1 Reciprocating Pin-on-flat Problem

A two-dimensional problem is first considered that corresponds, in a simplified manner, to the reciprocating pin-on-flat tribological test. This example is aimed at illustrating the concept of separation of time scales, as discussed in Sect. 4.2.

An elastic pin is pressed into an elastic block and a reciprocating motion is enforced under constant normal force, see Fig. 5 for the geometry and finite-element mesh used in the computations. Both the pin and the block undergo finite deformations and finite configuration changes due to wear. Details concerning geometry, frictional contact and material parameters can be found in Lengiewicz and Stupkiewicz (2012).

The formulation and the computational treatment rely here on the concept of two time scales and time-scale separation. The fast time scale τ corresponds to one loading cycle during which the pin is slid to the right and to the left with a fixed amplitude A, starting at the center of the block. The deformation subproblem that is solved at each slow time scale instant t includes an initial stage during which the

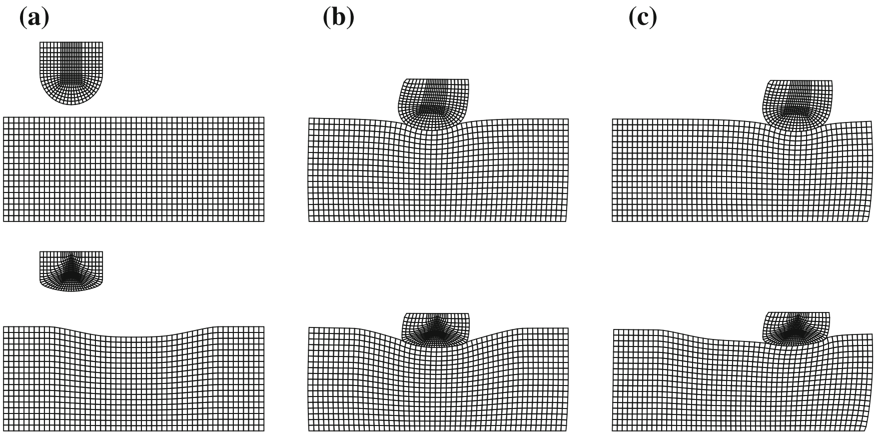

Fig. 5 Reciprocating pin-on-flat problem: initial (unworn, *top*) and final (worn, *bottom*) undeformed and deformed configurations at the beginning of the initial stage (**a**), at the beginning of the actual loading cycle (**b**), and in the right-most position after one quarter of the loading cycle (**c**) (reproduced from Lengiewicz and Stupkiewicz 2012)

pin is brought to contact in the left-most position, Fig. 5a, and then it is slid towards the center of the block, Fig. 5b. This ensures that the actual loading cycle starts in the condition of fully developed frictional sliding. Subsequently, the pin is slid the distance of A to the right, Fig. 5c, then the distance of $2A$ to the left, and finally the distance of A to the right, which completes the loading cycle in a single deformation subproblem. Following the assumption of scale separation, shape changes due to wear are suppressed at the fast time scale. After the deformation subproblem is solved and the corresponding wear increment is computed, the shape evolution subproblem is solved, here using the explicit scheme. The resulting finite shape changes are clearly visible in Fig. 5.

A study of accuracy of the explicit time integration scheme, including also the second-order explicit scheme that employs sensitivity analysis, can be found in Lengiewicz and Stupkiewicz (2012).

5.2 *Elastic Ball–Rigid Flat Problem*

In this example, an elastic ball is slid against a rigid surface under constant normal load, see Stupkiewicz (2013) for a detailed description. The problem is thus a quasi-steady-state wear problem, and the deformation subproblem is a steady-state frictional contact problem in a frame attached to the ball, cf. Sect. 4.3.

The ball radius is $R = 5\,\text{mm}$, the elastic properties are specified by $E = 100\,\text{GPa}$ and $\nu = 0.3$, and the normal force is $F = 100\,\text{N}$. Considering that the counter-body is rigid, the reduced elastic stiffness of the contact pair is approximately equal to that of two elastic bodies made of steel. The Hertzian pressure is then $p_0 = 2.1\,\text{GPa}$, and the Hertzian contact radius is $a = 0.15\,\text{mm}$. These are realistic conditions that correspond to the small-deformation regime. A finite-deformation counterpart has also been studied by Stupkiewicz (2013)—the corresponding results are not provided here.

Loading is applied at the mid-plane of the ball so that only one quarter of the ball can be analyzed considering the symmetry with respect to a plane parallel to the sliding direction. As the elastic strains are small, the undeformed and deformed configurations are very close one to the other. Note that frictional contact is here considered. Otherwise the problem would be axially symmetric. The initial and the final shape of the ball are shown in Fig. 6.

The contact pressure at two instants is shown in Fig. 7. The initial pressure at $t = 0$ is not included in Fig. 7 because the finite-element mesh is too coarse to reasonably reproduce the Hertzian pressure distribution (the element size in the contact area is 0.125 mm, while the Hertzian contact radius is $a = 0.15\,\text{mm}$). It can be seen that the pressure is uniform, and its value decreases as the contact area increases due to progressive wear. This response is easily explained by observing that the counter-surface is planar and rigid. As the elastic strains and displacements are small, the worn contact surface is also planar, see Fig. 6b. Accordingly, wear induces a kind of rigid-body motion of the ball in the normal direction. This rigid-body motion is then associated with a uniform wear rate which, through the wear model, induces a uniform contact pressure. Note that the related features of the quasi-steady-state wear problems constitute the basis for simplified asymptotic models (e.g., Paczelt and Mróz 2005; Lengiewicz and Stupkiewicz 2013).

The results reported above were obtained using the implicit scheme with a fixed time increment $\Delta t = 100\,\text{s}$ (actually, at the very beginning of the process, substepping was needed to achieve convergence so that 17 time steps were needed in total to complete the simulation). By numerical experiments, the critical time increment of the explicit time integration scheme has been estimated to be approximately equal to $\Delta t_{cr} \approx 0.1\,\text{s}$. Accordingly, the explicit scheme would require about 10,000 time

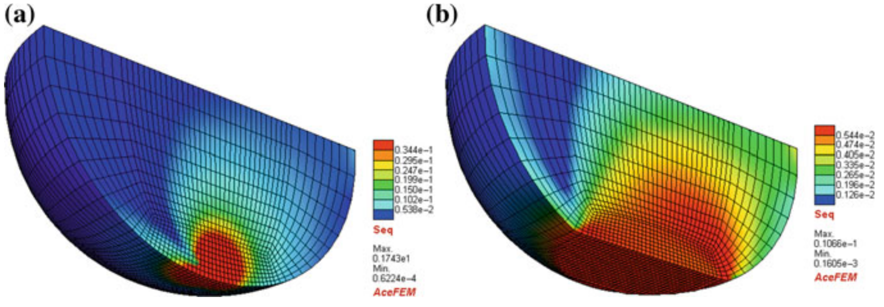

Fig. 6 Elastic ball–rigid flat problem: equivalent stress σ_{eq} in the deformed configuration (the undeformed configuration is nearly identical) at the initial time $t = 0$ (**a**) and at the final time $t = 1000\,\text{s}$ (**b**) (reproduced from Stupkiewicz 2013)

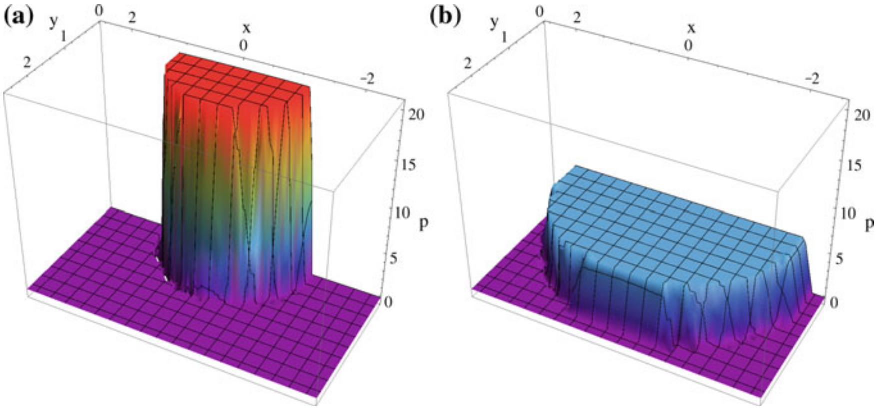

Fig. 7 Elastic ball–rigid flat problem: contact pressure (in MPa) at $t = 100\,\mathrm{s}$ (**a**) and $t = 1000\,\mathrm{s}$ (**b**) (reproduced from Stupkiewicz 2013)

steps to complete the simulation. Even though the computational cost of one time increment in the implicit scheme is higher than that of the explicit scheme due to the increased number of global unknowns, the implicit scheme is more efficient than the explicit one, and the gain in computational cost is significant (about two orders of magnitude).

5.3 *Rigid Ball Sliding Against Elastic Half-Space*

In this example, a rigid ball is repeatedly slid against an elastic half-space, see Stupkiewicz (2013) for details. Wear due to repeated sliding will thus result in formation of a wear groove on the half-space. This arrangement corresponds, for instance, to the ball-on-disk test, provided the curvature of the sliding path (and wear groove) on the disk is negligible. The problem is a quasi-steady-state problem so that the elastic half-space can be analyzed in an Eulerian frame with the coordinate system attached to the rigid ball. Specifically, an Eulerian description of the rigid-body motion in the undeformed configuration is adopted, while the deformation due to the contact interaction is treated in a Lagrangian manner, see Sect. 4.3. Other relevant tribological tests are illustrated in Fig. 8. In the case of the reciprocating pin-on-flat test, the periodic pin-on-flat arrangement is only an approximation since this problem is actually not a quasi-steady-state problem.

Referring to the pin-on-disk test, the disk wears due to the repeated contact at each revolution of the disk. Hence, the wear rate governing the evolution of the wear groove must be averaged along the sliding path, and the corresponding parameter L, the sliding length per cycle, must be specified. In the case of the pin-on-disk test, L is the circumference of the circular sliding path. This parameter is independent from

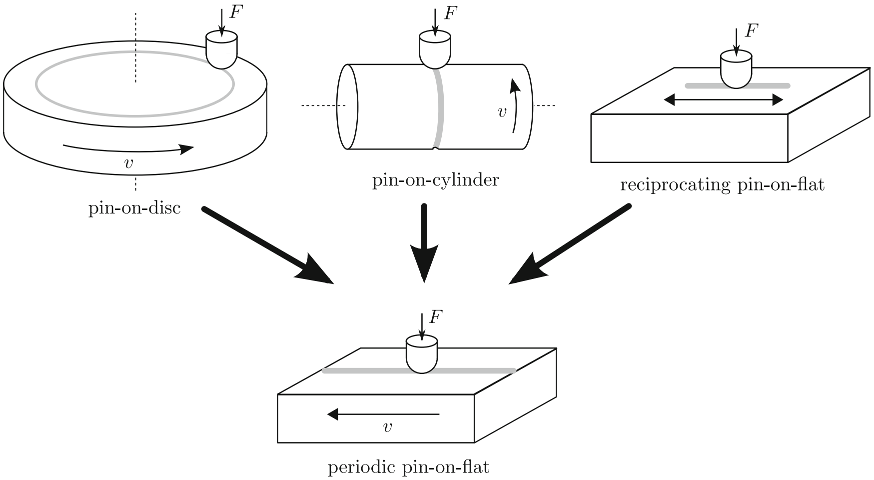

Fig. 8 Periodic pin-on-flat arrangement as an approximation of three tribological tests (reproduced from Lengiewicz and Stupkiewicz 2013)

the actual dimensions of the computational domain, the latter being restricted to the neighbourhood of the contact zone in order to reduce the computational cost.

Two sets of material parameters are considered that correspond to the finite-deformation and the small-deformation regime. Details are provided in Stupkiewicz (2013). The deformed finite-element mesh and the contact pressure at the initial and final time instant are shown in Fig. 9 for the case of the finite-deformation regime.

The wear groove is here uniform along the sliding direction which is a consequence of quasi-steady-state conditions. Accordingly, the shape transformation mapping $\boldsymbol{\Psi}$ is also uniform along the sliding direction, and it is sufficient to prescribe it as a two-dimensional field at one cross-section only. The number of corresponding degrees of freedom in the finite-element model is thus a small fraction of the total number of degrees of freedom, and the additional computational cost of solving the coupled problem of deformation and shape evolution, as referred to the cost of the deformation problem alone, is small. The fully coupled implicit scheme is thus particularly attractive for this class of problems.

In the finite-deformation regime, conditional stability of the explicit scheme is not a crucial issue, as already illustrated in the previous examples. The situation is again very different in the case of the small-deformation regime. Figure 10a presents the corresponding evolution of the contact pressure obtained using the implicit scheme. Initially, the Hertzian pressure distribution corresponds to the initial circular contact zone. Once the wear groove forms, the contact zone becomes elongated and so is the contact pressure distribution. A characteristic feature of the pressure distribution is observed for $t \geq 100\,\text{s}$ which results from the elastic contact interaction of the ball with a nearly cylindrical groove. Specifically, the pressure profile is uniform along the direction perpendicular to the sliding direction, except at the outer edge where

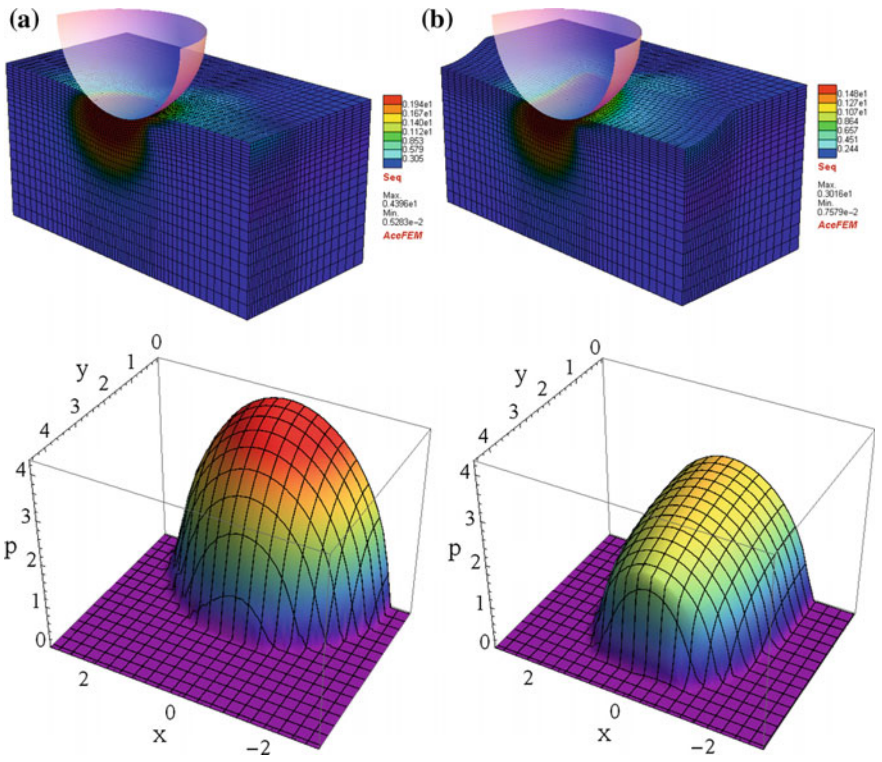

Fig. 9 Rigid ball–elastic half-space problem in the finite-deformation regime: equivalent stress σ_{eq} in the deformed configuration (*top*) and contact pressure (*bottom*) at (**a**) $t = 0$ and (**b**) $t = 1000$ s (reproduced from Stupkiewicz 2013)

a small pressure spike is formed. This pressure distribution is shown in detail at the bottom of Fig. 10a.

In this example, the finite-element mesh (not shown, see Stupkiewicz (2013)) consists of 65,600 hexahedral elements, and the total number of unknowns is 219,432 of which only about 3,400 are the displacement-like quantities corresponding to the shape transformation mapping $\boldsymbol{\Psi}$. The additional computational cost related to the application of the implicit time integration scheme is thus very small. This is because the number of additional unknowns associated with the shape transformation mapping is small compared to the total number of unknowns (less than 2%). The benefit due to stability of the integration scheme is thus obvious. Specifically, it has been checked that the critical time increment of the explicit scheme is here not greater than 0.5–1 s, thus at least 1000–2000 time steps would be needed to obtain a stable solution using the explicit scheme. The corresponding computational cost would thus be approximately two orders of magnitude higher than that of the implicit scheme for which the simulation required only 26 time steps.

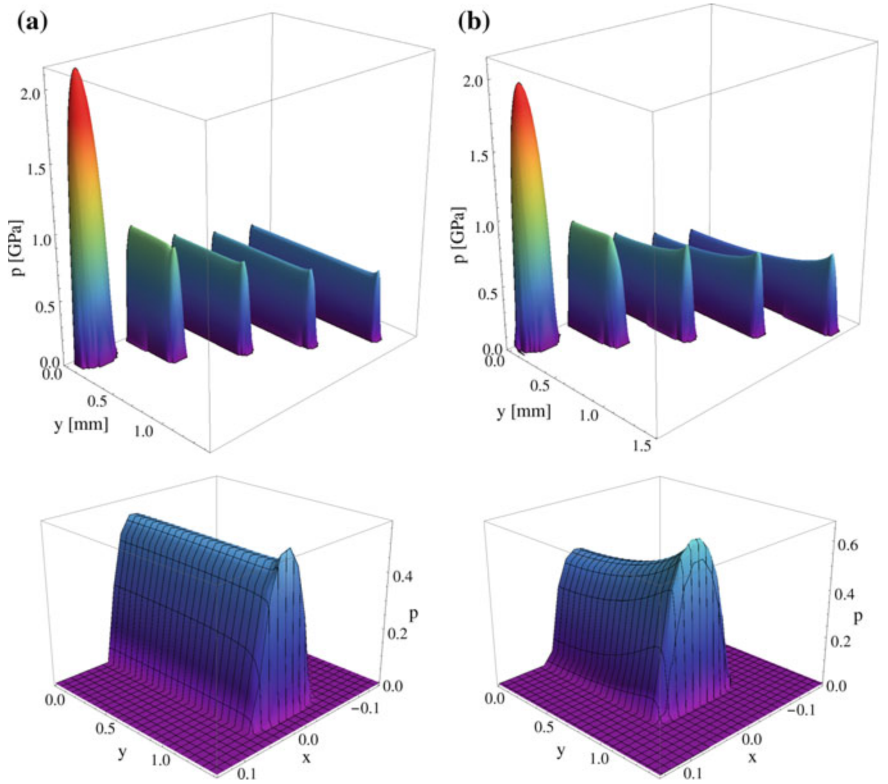

Fig. 10 Rigid ball–elastic half-space problem in the small-deformation regime for the homogeneous (**a**) and inhomogeneous (**b**) half-space. Top figures show evolution of the contact pressure (subsequent graphs correspond to $t = 0, 50, 200, 500, 1000\,\mathrm{s}$) and a detailed view of the contact pressure at $t = 1000\,\mathrm{s}$ is shown in the bottom figures. Results corresponding to the homogeneous half-space are reproduced from Stupkiewicz (2013)

Additional results obtained for an inhomogeneous surface layer are also included in Fig. 10b. Here, it is assumed that the elastic half-space is coated with a functionally graded (FGM) layer in which the elastic modulus and the wear coefficient depend on the depth. Both parameters increase linearly towards the surface starting from their reference values characteristic for the homogeneous substrate. As the material is removed and the wear groove is formed, the material characterized by a lower elastic modulus and a lower wear coefficient is thus gradually exposed. The local wear coefficient is thus non-uniform across the wear groove. As a result, the contact pressure increases towards the groove edges where the wear coefficient is the highest, see Fig. 10b.

5.4 Finite Wear: Summary

In Sects. 3, 4 and 5, a class of non-standard finite-wear contact problems has been discussed, and, in particular, illustrative numerical examples have been presented in Sects. 4.4 and 5.

The distinctive feature of the formulation proposed by Lengiewicz and Stupkiewicz (2012) and described in Sect. 4 is that finite changes of configuration are considered that result from both wear and deformation. This general setting implies that some care must be taken when formulating the problem. For instance, a distinction is made between the nominal and the spatial wear rate, and the wear law, e.g., the classical Archard law, must be adequately formulated, as discussed in Sect. 3. Also, the finite configuration changes have consequences for the finite-element treatment, here discussed in the context of the master-slave approach.

As the second important ingredient, the concept of two time scales has been introduced with the fast time scale of the deformation subproblem and the slow time scale corresponding to the shape evolution problem. Now, assuming separation of the two time scales allows one to partially decouple the two subproblems. Importantly, upon adopting this assumption, the deformation subproblem becomes a standard frictional contact problem which is not affected by the shape changes due to wear and thus can be solved using standard techniques of computational contact mechanics. This has been illustrated by the reciprocating pin-on-flat problem in Sect. 5.1.

Finally, the concept of two time scales provides a framework for developing various computational strategies for time integration of the shape evolution problem. The most common approach is based on applying the explicit forward-Euler scheme which is easy to implement, but which suffers from conditional stability. Alternative strategies include the approach employing the unconditionally-stable implicit backward-Euler scheme that has been studied in Sect. 4.4 and successfully applied to more advanced problems in Sects. 5.2 and 5.3. In particular, in the case of the rigid ball–elastic half-space problem, a high-quality solution of this three-dimensional problem has been obtained at a relatively low computational cost thanks to the application of the implicit scheme. To the best of our knowledge, similar results are not available in the literature, and this is because the application of the usual explicit time-integration scheme would be associated with a very high computational cost due to the severe constraint on the time step, as imposed by the stability criterion.

6 Hydrodynamic Lubrication

6.1 Introduction to Soft-EHL

Hydrodynamic lubrication is a contact regime in which the contacting solids are fully separated by a thin film of fluid (lubricant) such that the load is fully transferred by the hydrodynamic pressure that develops in the fluid. When the hydrodynamic pressure is sufficiently high to elastically deform the contacting bodies, the thickness of the gap between the bodies changes, which in turn influences the fluid flow. This introduces the elasto-hydrodynamic coupling which is characteristic for the elasto-hydrodynamic lubrication (EHL) regime. Finally, when one or both contacting bodies are highly compliant (or soft), a relatively low pressure suffices to significantly deform the bodies, and this lubrication regime is usually called *soft-EHL*. Alternatively, it is called *elastic-isoviscous* regime, as the effect of the pressure dependence of fluid viscosity is not essential, and the viscosity can be assumed constant, contrary to the elastic-piezoviscous (or hard-EHL) regime in which the related effects are crucial. The focus of the remainder of this chapter is on the soft-EHL problems and, in particular, on the related finite-deformation effects.

Representative examples of soft-EHL problems include elastomeric seals, windscreen wipers, wet tyres, and others. However, the soft-EHL regime is also characteristic for many biotribological systems, such as synovial joints, contact-lens lubrication, eye–eyelid contact, human skin contact, and oral processing of food (e.g., Dowson 1995; de Vicente et al. 2005; Adams et al. 2007; Jones et al. 2008). Clearly, additional difficulties are encountered in the modelling of biotribological systems, which are associated with the modelling of the complex constitutive behaviour of soft tissues and biological fluids. The related effects are not discussed here.

In the context of hydrodynamic lubrication, the fluid flow in the thin channel between the contacting bodies is usually described using the well-known Reynolds equation (Reynolds 1886). The Reynolds equation is obtained from the Navier–Stokes equation by integrating it over the film thickness under several assumptions of which the most important one is that the film is thin so that the flow is laminar and fluid inertia is negligible (Dowson and Higginson 1977; Hamrock et al. 2004). The resulting partial differential equation, introduced in Sect. 6.3 below, relates the hydrodynamic pressure (assumed constant across the film) and the film thickness. In the usual setting, the film thickness is assumed known, and unknown is the pressure. Transition from the Navier–Stokes equation to the Reynolds equation is associated with a dimension reduction so that the Reynolds equation is formulated on the lubrication surface, and the corresponding problem is thus two-dimensional in the general three-dimensional case.

Two phenomena are considered in the modelling of an EHL problem, namely the fluid flow in the thin channel between the contacting bodies and the elastic deflections of the bodies. As mentioned above, the fluid subproblem is conveniently modelled using the Reynolds equation that relates the hydrodynamic pressure and the film thickness. At the same time, the film thickness is influenced by the elastic deflections of the bodies as a result of the action of the hydrodynamic pressure. The two subproblems are thus strongly coupled.

The EHL problem is thus, in fact, a particular kind of a fluid–structure interaction (FSI) problem in which the fluid part is modelled using the Reynolds equation upon adopting the thin-film approximation. In principle, the general FSI approach can alternatively be applied, in which the Navier–Stokes equation is directly used for the fluid part. This general approach offers several advantages by relaxing the assumptions behind the Reynolds equation. At the same time, whenever those assumptions are reasonably satisfied, the two approaches yield similar results (e.g., Almqvist et al. 2004; Hajishafiee et al. 2017), while the approach based on the Reynolds equation is expected to be significantly more efficient due to the reduced number of degrees of freedom and due to the ease of spatial discretization.

In the classical EHL theory, the solid subproblem is modelled within the linear-elasticity framework. The elasticity problem is then usually formulated for a half-space so that specialized, highly efficient solution methods can be applied (Dowson and Higginson 1977; Hamrock et al. 2004). While both assumptions (linear elasticity, half-space approximation) are well justified in the case of the hard-EHL problems, this is not necessarily so in the case of the soft-EHL problems in which finite deformations may be encountered. Furthermore, the size of the contact zone may be comparable to the size of the contacting bodies so that the half-space approximation is then not adequate.

In realistic conditions, the lubricant film is very thin so that surface roughness may significantly influence the fluid flow and the overall behaviour of the contact pair. However, the related effects are not discussed in the following, and the presentation of the Reynolds equation is restricted to the case of smooth surfaces. Let us only mention here that several approaches are readily available for the modelling of roughness effects through the so-called flow factors introduced first by Patir and Cheng (1978) and reinterpreted later in the rigorous framework of the homogenization theory (Bayada and Faure 1989; Buscaglia and Jai 2000; Bou-Said and Kane 2004; Bayada et al. 2006; Almqvist et al. 2011; Waseem et al. 2017).

6.2 Lubrication Surface and Film Thickness

The Reynolds equation is usually formulated on a planar lubrication surface. Below, a more general form is provided for a non-planar surface. The presentation is here restricted to a time-independent lubrication surface, while the general case of a time-dependent lubrication surface is discussed in detail in the recent work of Temizer and Stupkiewicz (2016).

Let us consider the flow of a fluid (lubricant) in a thin channel between two *physical surfaces* $\gamma_l^{(i)}$, $i = 1, 2$, that represent the contact boundaries of the two contacting bodies in the current configuration, see Fig. 11. The physical surface $\gamma_l^{(i)}$ is parametrized by the convected curvilinear coordinates $\xi^{(i),\alpha}$, $\alpha = 1, 2$, so that the position of a material point in the current configuration is represented by $\mathbf{x}^{(i)} = \mathbf{x}^{(i)}(\boldsymbol{\xi}^{(i)}, t)$ for $\mathbf{x}^{(i)} \in \gamma_l^{(i)}$.

We also introduce the *lubrication surface* $\mathcal{S}$ on which the lubricant flow will be described. It is assumed that the lubrication surface $\mathcal{S}$ is located between the physical surfaces $\gamma_l^{(i)}$. This imposes a constraint on the deformation (motion) of the physical surfaces because $\mathcal{S}$ is here assumed time-independent. Actually, the case of the time-independent lubrication surface is most relevant when one of the physical surfaces is rigid so that the lubrication surface can be identified with this rigid surface.

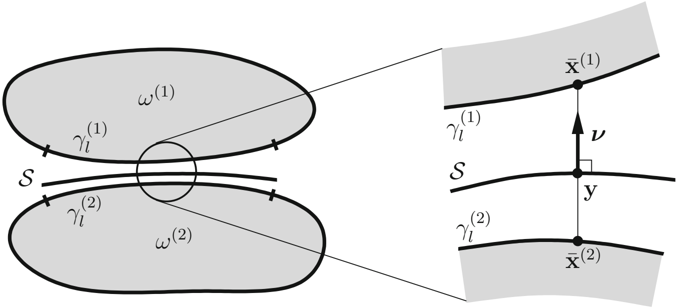

Fig. 11 Physical surfaces $\gamma_l^{(i)}$ and lubrication surface $\mathcal{S}$

Note that there is some ambiguity in the choice of the location of the lubrication surface $\mathcal{S}$ between the physical surfaces $\gamma_l^{(i)}$ when the distance between the physical surfaces is finite (though still sufficiently small so that the Reynolds approximation holds). The results of the computational study reported by Stupkiewicz et al. (2016), see also Fig. 23, show that the solution of the EHL problem is not much afftected by the location of the lubrication surface, and this aspect is not discussed here in detail.

Position of a point on the lubrication surface $\mathcal{S}$ is denoted by $\mathbf{y}$, and parametrization of $\mathcal{S}$ by curvilinear coordinates $\boldsymbol{\eta} = \{\eta^1, \eta^2\}$ is introduced so that $\mathbf{y} = \mathbf{y}(\boldsymbol{\eta})$ for $\mathbf{y} \in \mathcal{S}$. This parametrization introduces the tangent basis $\mathbf{g}_\alpha$ and the co-basis $\mathbf{g}^\alpha$ such that

$$\mathbf{g}_\alpha = \frac{\partial \mathbf{y}}{\partial \eta^\alpha}, \qquad \mathbf{g}^\alpha \cdot \mathbf{g}_\beta = \delta^\alpha_\beta, \qquad \alpha, \beta = 1, 2, \tag{32}$$

where δ^α_β is the Kronecker delta. Let $\boldsymbol{\nu}$ denote the unit normal to $\mathcal{S}$, pointing in the direction from $\gamma_l^{(2)}$ to $\gamma_l^{(1)}$, thus $\mathbf{g}_\alpha \cdot \boldsymbol{\nu} = 0$.

Consider now a scalar field $\phi = \phi(\boldsymbol{\eta})$ defined on $\mathcal{S}$. The *surface gradient* of ϕ can be expressed as

$$\operatorname{grad}_{\mathcal{S}} \phi = \frac{\partial \phi}{\partial \eta^\alpha} \mathbf{g}^\alpha, \tag{33}$$

where the repeated (Greek) indices are implicitly summed over. It follows that the surface gradient of a scalar field is a vector tangent to $\mathcal{S}$. Similarly, the *surface divergence* of a vector field $\boldsymbol{\phi} = \boldsymbol{\phi}(\boldsymbol{\eta})$ defined on $\mathcal{S}$ can be expressed as

$$\operatorname{div}_{\mathcal{S}} \boldsymbol{\phi} = \frac{\partial \boldsymbol{\phi}}{\partial \eta^\alpha} \cdot \mathbf{g}^\alpha. \tag{34}$$

For future use, we also recall the *surface-divergence theorem* for a continuously differentiable *tangential* vector field $\boldsymbol{\phi}$ (thus $\boldsymbol{\phi} \cdot \boldsymbol{\nu} = 0$),

$$\int_{\mathcal{S}} \operatorname{div}_{\mathcal{S}} \boldsymbol{\phi} \, \mathrm{d}s = \int_{\partial\mathcal{S}} \boldsymbol{\phi} \cdot \mathbf{m} \, \mathrm{d}l, \tag{35}$$

where $\mathbf{m}$ is a unit vector tangent to $\mathcal{S}$ that is simultaneously an outward normal to $\partial\mathcal{S}$.

One of the basic assumptions in the derivation of the Reynolds equation is that the thickness of the lubricant film, denoted by $h = h(\boldsymbol{\eta}, t)$, is small compared to the dimensions of the lubrication surface $\mathcal{S}$. Even though the present formulation admits finite deformations of the contacting bodies, the above assumption restricts those deformations such that the film thickness is sufficiently small so that the Reynolds approximation holds. In typical conditions, the film thickness is indeed small except in the inlet and outlet zones in which the two contacting surfaces diverge and the film thickness may no longer be small. However, the hydrodynamic pressure buildup is concentrated in the zone where the film thickness is relatively small (note that the Poiseuille term discussed below depends on h^3). Accordingly, even if the film thickness is relatively large in the inlet and outlet zones, and thus the assumption of small film thickness may be violated there, the related effect on the solution in the actual contact zone is not substantial.

Since the fluid film thickness is here considered finite, though small, there is some ambiguity in defining its measure. In the following we adopt the definition based on the *inverse-orthogonal* projection, as illustrated in Fig. 11, but alternative options are also possible (cf. Temizer and Stupkiewicz 2016). The film thickness h is thus decomposed into the measures $h^{(i)}$ of the gap between the physical surfaces $\gamma_l^{(i)}$ and the lubrication surface $\mathcal{S}$,

$$h = h^{(1)} - h^{(2)}, \tag{36}$$

where $h^{(i)}$ is defined by the inverse-orthogonal projection of a point $\mathbf{y} \in \mathcal{S}$ onto $\gamma_l^{(i)}$ along the normal $\boldsymbol{\nu}$,

$$h^{(i)} = (\bar{\mathbf{x}}^{(i)} - \mathbf{y}) \cdot \boldsymbol{\nu}. \tag{37}$$

Here, $\bar{\mathbf{x}}^{(i)} = \mathbf{x}^{(i)}(\bar{\boldsymbol{\xi}}^{(i)}, t)$ is the inverse-orthogonal projection of $\mathbf{y}$ onto $\gamma_l^{(i)}$, defined such that $\bar{\mathbf{x}}^{(i)} = \mathbf{y} + h^{(i)}\boldsymbol{\nu}$, and a bar over the symbol denotes the quantity evaluated at the projection point.

6.3 Reynolds Equation

The Reynolds equation expresses the mass balance of the fluid contained in the thin channel between the physical surfaces $\gamma_l^{(1)}$ and $\gamma_l^{(2)}$ (e.g., Hamrock et al. 2004). For a time-independent non-planar lubrication surface $\mathcal{S}$, the mass balance equation takes the following form:

$$\frac{\partial(\varrho h)}{\partial t} + \operatorname{div}_{\mathcal{S}}(\varrho \mathbf{q}) = 0, \tag{38}$$

where $\mathbf{q}$ is the fluid flux vector tangent to $\mathcal{S}$, to be specified below, and ϱ is the density.

For an *incompressible* fluid (relevant for the soft-EHL), the density ϱ is constant and the Reynolds equation expresses the balance of volume, viz.

$$\frac{\partial h}{\partial t} + \operatorname{div}_{\mathcal{S}} \mathbf{q} = 0. \tag{39}$$

In the Reynolds approximation of the fluid flow within the thin film, the fluid flux $\mathbf{q}$ comprises two components: the Poiseuille term is proportional to the pressure gradient and corresponds to the parabolic profile of the fluid velocity across the film, while the Couette term is proportional to the average tangential velocity, see Fig. 12. Specifically, the fluid flux is given by the following expression,

$$\mathbf{q} = -\frac{h^3}{12\mu} \operatorname{grad}_{\mathcal{S}} p + h \mathbf{v}_T, \tag{40}$$

where p is the pressure, $\mathbf{v}_T$ is the mean tangential velocity of the two physical surfaces, and μ is the fluid viscosity, which is here assumed constant, but its pressure-dependence can be easily accounted for. It is recalled that the Reynolds equation is formulated on the lubrication surface $\mathcal{S}$ so that all quantities depend on the curvilinear coordinates $\boldsymbol{\eta}$ and time, thus, for instance, $p = p(\boldsymbol{\eta}, t)$.

In view of the kinematics introduced by the inverse-orthogonal projection and by the definition of the film thickness h, Eqs. (36)–(37), the mean tangential velocity $\mathbf{v}_T$ is defined as

$$\mathbf{v}_T = \frac{1}{2}\left(\bar{\mathbf{v}}_T^{(1)} + \bar{\mathbf{v}}_T^{(2)}\right), \tag{41}$$

where $\bar{\mathbf{v}}_T^{(i)} = \mathbf{v}^{(i)}(\bar{\boldsymbol{\xi}}^{(i)}, t)$ is the tangential velocity of the physical surface $\gamma_l^{(i)}$ at the projection point $\bar{\mathbf{x}}^{(i)}$,

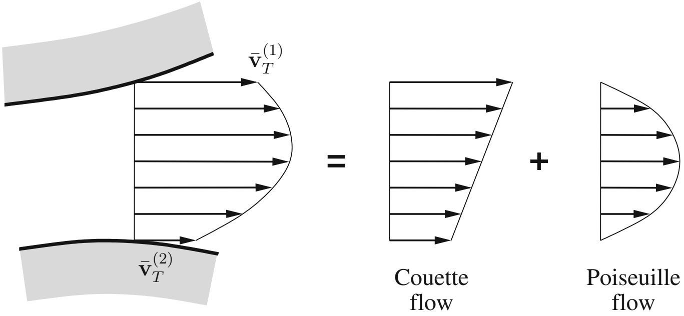

Fig. 12 Fluid velocity across a thin channel: Couette and Poiseuille contributions

$$\mathbf{v}_T^{(i)} = \mathbf{v}^{(i)} - v_N^{(i)} \boldsymbol{\nu}, \qquad \mathbf{v}^{(i)} = \frac{\partial \mathbf{x}^{(i)}}{\partial t}, \qquad v_N^{(i)} = \mathbf{v}^{(i)} \cdot \boldsymbol{\nu}. \tag{42}$$

The Reynolds equation (39)–(40) is accompanied by the standard essential and natural boundary conditions, namely

$$p = p^* \quad \text{on } \partial_p \mathcal{S} \qquad \text{and} \qquad \mathbf{q} \cdot \mathbf{m} = q^* \quad \text{on } \partial_q \mathcal{S}, \tag{43}$$

where p^* is the pressure prescribed on the boundary $\partial_p \mathcal{S}$, q^* is the flux prescribed on the boundary $\partial_q \mathcal{S}$, and $\mathbf{m}$ is a unit vector tangent to $\mathcal{S}$ and normal to $\partial \mathcal{S}$, pointing outwards of $\mathcal{S}$. Note that cavitation, if considered, introduces additional boundary conditions on an unknown cavitation boundary, see Remark 3.1.

The first term in the Reynolds equation (39) is the time derivative of the film thickness $h = h(\boldsymbol{\eta}, t)$. This derivative is evaluated at fixed $\boldsymbol{\eta}$ and, in view of Eqs. (36)–(37), it involves differentiation of the position $\bar{\mathbf{x}}^{(i)}$ of the projection point (for fixed $\boldsymbol{\eta}$). Note that the coordinates $\bar{\boldsymbol{\xi}}^{(i)}$ of the projection point depend on time so that we have $\bar{\mathbf{x}}^{(i)} = \mathbf{x}^{(i)}(\bar{\boldsymbol{\xi}}^{(i)}(\boldsymbol{\eta}, t), t)$. The time derivative of $h^{(i)}$ at fixed $\boldsymbol{\eta}$ is thus equal to

$$\frac{\partial h^{(i)}}{\partial t} = \left(\bar{\mathbf{v}}^{(i)} + \frac{\partial \mathbf{x}^{(i)}}{\partial \xi^{(i),\alpha}} \dot{\bar{\xi}}^{(i),\alpha} \right) \cdot \boldsymbol{\nu} = \bar{v}_N^{(i)} + (\bar{\boldsymbol{\tau}}_\alpha^{(i)} \cdot \boldsymbol{\nu}) \, \dot{\bar{\xi}}^{(i),\alpha}, \tag{44}$$

where $\boldsymbol{\tau}_\alpha^{(i)}$ denotes the tangent basis associated with the parametrization of the physical surface $\gamma_l^{(i)}$ by $\boldsymbol{\xi}^{(i)}$, and we have

$$\frac{\partial h}{\partial t} = \bar{v}_N^{(1)} - \bar{v}_N^{(2)} + \left(\bar{\boldsymbol{\tau}}_\alpha^{(1)} \dot{\bar{\xi}}^{(1),\alpha} - \bar{\boldsymbol{\tau}}_\alpha^{(2)} \dot{\bar{\xi}}^{(2),\alpha} \right) \cdot \boldsymbol{\nu}. \tag{45}$$

Note that, in general, $\bar{\boldsymbol{\tau}}_\alpha^{(i)} \cdot \boldsymbol{\nu} \neq 0$ since the physical surfaces are not necessarily parallel to the lubrication surface. It follows from Eq. (45) that the time derivative of the film thickness h involves not only the normal velocities $\bar{v}_N^{(i)}$ of the physical surfaces, but also the term related to the motion of the physical surfaces that are (locally) inclined with respect to the lubrication surface. This is further discussed in Sect. 6.6 in the case of a planar lubrication surface.

For future use, we provide here the formula for the surface traction acting on the physical surface $\gamma_l^{(i)}$:

$$\mathbf{t}^{(i)} = -p\mathbf{n}^{(i)} - \frac{\mu}{h} \left(\bar{\mathbf{v}}_T^{(i)} - \bar{\mathbf{v}}_T^{(i\pm1)} \right) - \frac{h}{2} \operatorname{grad}_{\mathcal{S}} p, \tag{46}$$

where $\mathbf{n}^{(i)}$ is the unit outward normal to $\gamma_l^{(i)}$. The first term is the normal traction due to the hydrodynamic pressure. The second and the third term are due to the viscous shear stresses in the fluid that act on the solid surfaces (Hamrock et al. 2004, Sect. 7.3). Specifically, the second term results from the Couette flow, and $\bar{\mathbf{v}}_T^{(i\pm1)}$ denotes here the tangential velocity of the countersurface, i.e. $i \pm 1 = 2$ for $i = 1$ and $i \pm 1 = 1$ for $i = 2$. Accordingly, the second term is proportional to the tangential relative velocity, and it acts on the two surfaces in the opposite direction. The third term results from the Poiseuille flow. This term is proportional to the pressure gradient, and it acts on the two surfaces in the same direction.

6.4 Weak Form of the Reynolds Equation

The weak form of the Reynolds equation (39) is obtained by following the standard procedure. Equation (39) is first multiplied by a test function δp, which vanishes on $\partial_p \mathcal{S}$, and integrated over the lubrication surface $\mathcal{S}$, thus

$$\int_{\mathcal{S}} \left(\frac{\partial h}{\partial t} + \mathrm{div}_{\mathcal{S}}\, \mathbf{q} \right) \delta p \, \mathrm{d}s = 0 \qquad \forall\, \delta p. \tag{47}$$

By using the identity

$$\mathrm{div}_{\mathcal{S}}(\mathbf{q}\,\delta p) = (\mathrm{div}_{\mathcal{S}}\, \mathbf{q})\delta p + \mathbf{q} \cdot \mathrm{grad}_{\mathcal{S}}\, \delta p \tag{48}$$

and by applying the divergence theorem (34) to the term $\mathrm{div}_{\mathcal{S}}(\mathbf{q}\,\delta p)$, Eq. (47) is then transformed to the following weak form,

$$\int_{\mathcal{S}} \left(\frac{\partial h}{\partial t} \delta p - \mathbf{q} \cdot \mathrm{grad}_{\mathcal{S}}\, \delta p \right) \mathrm{d}s + \int_{\partial_q \mathcal{S}} q^* \delta p \, \mathrm{d}l = 0 \qquad \forall\, \delta p, \tag{49}$$

where the boundary integral over $\partial_p \mathcal{S}$ vanishes because the test function δp vanishes on $\partial_p \mathcal{S}$.

6.5 Cavitation

Cavitation is an important phenomenon in hydrodynamic lubrication, although, for highly compliant solids, the effect of cavitation on friction is limited (Persson and Scaraggi 2009). The popular mass-conserving cavitation model is briefly presented below. This model is often referred to as the JFO model as it follows the pioneering work of Jakobsson and Floberg (1957) and Olsson (1965). The formulation presented below is based on that developed by Lengiewicz et al. (2014), where more details can found, including the references to the earlier work.

When cavitation occurs, the lubrication surface $\mathcal{S}$ is divided into the full-film region $\mathcal{S}_f$ and the cavitated region $\mathcal{S}_c$ with the cavitation boundary, denoted by Σ, separating the two regions, cf. Fig. 13. The position of the cavitation boundary Σ constitutes a part of the solution hence the cavitation problem belongs to the class of free-boundary problems.

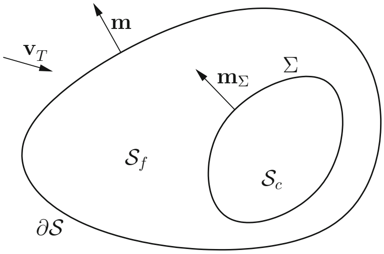

Fig. 13 Cavitation: full-film region $\mathcal{S}_f$ and cavitated region $\mathcal{S}_c$

Cavitation occurs when the hydrodynamic pressure drops to the cavitation pressure p_{cav}, and the pressure is constant and equal to the cavitation pressure $p = p_{cav}$ in the cavitated region, viz.

$$p \geq p_{cav} \ \text{ on } \mathcal{S} \qquad \text{and} \qquad p = p_{cav} \ \text{ on } \mathcal{S}_c. \tag{50}$$

In the cavitated region, the fluid is a mixture of liquid, vapor, and gas, and its density ϱ is thus lower than the density ϱ_0 of the intact fluid,

$$\varrho \leq \varrho_0 \ \text{ on } \mathcal{S} \qquad \text{and} \qquad \varrho = \varrho_0 \ \text{ on } \mathcal{S}_f. \tag{51}$$

Since the focus is here on soft-EHL problems, the intact fluid is assumed incompressible so that the density $\varrho = \varrho_0$ is constant in the full-film region $\mathcal{S}_f$. Introducing the relative density $\bar{\varrho} = \varrho/\varrho_0$ and assuming for simplicity that $p_{cav} = 0$, conditions (50) and (51) can be compactly written in the form of the following complementarity conditions,

$$p \geq 0, \qquad \bar{\varrho} - 1 \leq 0, \qquad p(\bar{\varrho} - 1) = 0 \qquad \text{on } \mathcal{S}, \tag{52}$$

which resemble the unilateral contact conditions (4).

Since the density is no longer constant, the Reynolds equation is now written in the following form, cf. Eq. (38),

$$\frac{\partial(\bar{\varrho}h)}{\partial t} + \operatorname{div}_{\mathcal{S}}(\bar{\varrho}\mathbf{q}) = 0, \tag{53}$$

In the full-film region $\mathcal{S}_f$ the flux is defined by Eq. (40), while in the cavitated region $\mathcal{S}_c$ the flux is assumed to comprise only the Couette term, thus

$$\mathbf{q} = h\mathbf{v}_T \quad \text{on } \mathcal{S}_c, \tag{54}$$

which can be formally obtained from Eq. (40) by putting $\operatorname{grad}_{\mathcal{S}} p = \mathbf{0}$, in agreement with the assumption that the pressure is constant in in the cavitated region.

The mass-balance equation (53) is accompanied by the continuity condition that enforces the mass balance on the cavitation boundary Σ,

$$(\bar{\varrho}^{+}\mathbf{q}^{+} - \bar{\varrho}^{-}\mathbf{q}^{-}) \cdot \mathbf{m}_{\Sigma} = 0 \quad \text{on } \Sigma, \tag{55}$$

where $\mathbf{m}_{\Sigma}$ is the unit vector tangent to $\mathcal{S}$, normal to Σ, and oriented outwards from $\mathcal{S}_c$. The superscripts '+' and '−' denote the limit values of the corresponding quantities as the cavitation boundary Σ is approached from the full-film and cavitated side, respectively.

The weak form of the Reynolds equation combined with the above mass-conserving cavitation model can by obtained by following the procedure outlined in Sect. 6.4, applied to the full-film region $\mathcal{S}_f$ and to the cavitation region $\mathcal{S}_c$ separately, and by exploiting the continuity condition (55). This leads to the following weak form

$$\int_{\mathcal{S}} \left(\frac{\partial(\bar{\varrho}h)}{\partial t}\, \delta p - \bar{\varrho}\mathbf{q} \cdot \mathrm{grad}_{\mathcal{S}}\, \delta p \right) \mathrm{d}s = 0 \qquad \forall\, \delta p, \tag{56}$$

where it has been additionally assumed that the Dirichlet boundary condition $(43)_1$ is prescribed on the whole boundary $\partial\mathcal{S}$ so that the boundary term vanishes. However, this form is not suitable for the finite-element implementation because it is not compatible with the upwind scheme that is needed to stabilize the advection equation in the cavitated region, see Remark 3.2 below.

An alternative weak form is obtained by applying the divergence theorem only to the pressure-gradient part of the flux $\mathbf{q}$, which yields the following weak form (Lengiewicz et al. 2014, Appendix A)

$$\int_{\mathcal{S}} \left(\frac{\bar{\varrho}h^3}{12\mu}\, \mathrm{grad}_{\mathcal{S}}\, p \cdot \mathrm{grad}_{\mathcal{S}}\, \delta p + \left(\mathrm{div}_{\mathcal{S}}(\bar{\varrho}\mathbf{v}_T h) + \frac{\partial(\bar{\varrho}h)}{\partial t} \right) \delta p \right) \mathrm{d}s \\ + \int_{\Sigma} (\bar{\varrho}^{+} - \bar{\varrho}^{-}) h \mathbf{v}_T \cdot \mathbf{m}_{\Sigma}\, \delta p\, \mathrm{d}l = 0. \tag{57}$$

We note that the last term in the above weak form involves the jump of the relative density $\bar{\varrho}$ along the cavitation boundary Σ. Actually, the relative density $\bar{\varrho}$ is continuous on the rupture boundary and suffers discontinuity on the reformation boundary, see Remark 3.1. Considering that the position of the cavitation boundary Σ is unknown, the jump term in the weak form (57) is an undesired feature from the point of view of finite-element implementation. In the approach developed by Lengiewicz et al. (2014), a continuous finite-element approximation of the relative density $\bar{\varrho}$ (actually, of the void fraction $\lambda = 1 - \bar{\varrho}$) has been introduced so that the jump term vanishes, and a direct finite-element treatment is possible. The jump of $\bar{\varrho}$ on the reformation boundary is then approximated by a continuous solution with a high gradient.

The lubrication and cavitation problem is governed by the weak form (57) and by the complementarity conditions (52). After a small modification, the problem can be formulated as a linear complementarity problem (LCP) that can be solved using the methods available for this class of problems (Giacopini et al. 2010). In the computational scheme developed by Lengiewicz et al. (2014), the complementarity conditions (52) are enforced by introducing a non-smooth constraint function that relates two independent unknown fields, the pressure p and the relative density $\bar{\varrho}$. This two-field formulation can be transformed to a single-field formulation in which a single variable is used, along with the complementarity conditions (57), to represent the two physical fields, see also Hajjam and Bonneau (2007). A single-field formulation is also employed in the classical Elrod–Adams cavitation algorithm (Elrod and Adams 1974; Elrod 1981) in which the fluid is assumed compressible in the full-film region so that the pressure and the density are related by a one-to-one function. The formulation outlined above is applicable for an incompressible fluid.

Remark 3.1 The mass-flux continuity condition (55) and the cavitation condition (52) imply the well-known boundary conditions of the JFO theory. Specifically, on the film rupture boundary, where $\mathbf{v}_T \cdot \mathbf{m}_\Sigma < 0$, the relative density $\bar{\varrho}$ is continuous so that we have

$$p^+ = 0 \quad \text{and} \quad (\text{grad}_{\mathcal{S}}\, p)^+ \cdot \mathbf{m}_\Sigma = 0. \tag{58}$$

On the reformation boundary, where $\mathbf{v}_T \cdot \mathbf{m}_\Sigma > 0$, the relative density $\bar{\varrho}$ suffers discontinuity which, in view of condition (55), implies discontinuity of the pressure gradient, thus

$$p^+ = 0 \quad \text{and} \quad \frac{\bar{\varrho}^+ h^3}{12\mu}(\text{grad}_{\mathcal{S}}\, p)^+ \cdot \mathbf{m}_\Sigma = (\bar{\varrho}^+ - \bar{\varrho}^-) h \mathbf{v}_T \cdot \mathbf{m}_\Sigma. \tag{59}$$

The formulation developed by Lengiewicz et al. (2014) and outlined above is based on the general continuity condition (55), and the boundary conditions (58) and (59) are not employed directly.

Remark 3.2 In the cavitated region, the lubrication and cavitation problem becomes a pure advection problem because the pressure gradient vanishes in that region in view of the condition $(50)_2$. The standard Galerkin finite-element formulations are not suitable for such problems (Zienkiewicz and Taylor 2000), and upwinding schemes are usually used to stabilize the problem. However, the popular streamline upwind/Petrov–Galerkin (SUPG) method (Brooks and Hughes 1982) is not effective in the case of the weak form (56), because it involves the test-function gradient, which is not affected by the upwind correction when low-order (linear) elements are used. Accordingly, the alternative weak form (57) is needed, for which the SUPG method works well, see Lengiewicz et al. (2014) for details.

6.6 *Traditional Form for a Planar Lubrication Surface*

The Reynolds equation is usually formulated on a planar lubrication surface, which also includes the case of an unwrapped cylindrical surface of a journal bearing. The compact vector notation employed so far in Sect. 6 is not popular either. For completeness, the traditional form of the Reynolds equation is thus included below.

Assume thus that the physical surface $\gamma_l^{(2)}$ is planar and so is the lubrication surface $\mathcal{S}$ which is represented by a domain in the (x, y)-plane so that the normal $\boldsymbol{\nu}$ is aligned with the z-axis. The Reynolds equation (39)–(40) can then be written in the following form:

$$\frac{\partial}{\partial x}\left(\frac{h^3}{12\mu}\frac{\partial p}{\partial x}\right)+\frac{\partial}{\partial y}\left(\frac{h^3}{12\mu}\frac{\partial p}{\partial y}\right) = \frac{\partial}{\partial x}\left(\frac{h}{2}\left(v_x^{(1)}+v_x^{(2)}\right)\right)+\frac{\partial}{\partial y}\left(\frac{h}{2}\left(v_y^{(1)}+v_y^{(2)}\right)\right)+\frac{\partial h}{\partial t}, \qquad (60)$$

where $v_x^{(i)}$, $v_y^{(i)}$ and $v_z^{(i)}$ are the components of the velocity $\mathbf{v}^{(i)}$. The time derivative of the film thickness h is now given by the following formula:

$$\frac{\partial h}{\partial t} = v_z^{(1)} - v_z^{(2)} - v_x^{(1)}\frac{\partial h}{\partial x} - v_y^{(1)}\frac{\partial h}{\partial y}, \qquad (61)$$

see (Hamrock et al. 2004, Sect. 7.3). As in the general case, cf. Eq. (45), in addition to the contribution of the normal velocity components $v_z^{(i)}$, $\partial h/\partial t$ comprises the term related to the tangential (in-plane) motion of an inclined physical surface $\gamma_l^{(1)}$. Note that $\gamma_l^{(2)}$ is assumed to be planar and parallel to the (x, y)-plane hence it does not contribute to $\partial h/\partial t$.

7 Formulation of the Soft-EHL Problem

This section presents the formulation and the finite-element treatment of the soft-EHL problem. The formulation and its implementation are restricted to steady-state conditions, and one of the contacting bodies is assumed to be rigid and is represented by a rigid surface. Finite deformations of the other body, which is assumed hyperelastic, are fully accounted for.

7.1 Solid Part

Consider first the solid subproblem formulated for the hyperelastic body ($i = 1$, the index is omitted in the following), the other body ($i = 2$) is assumed to be rigid. In the finite-deformation framework, the reference configuration Ω and the current configuration ω are introduced along with the deformation mapping $\mathbf{x} = \boldsymbol{\varphi}(\mathbf{X})$, where $\mathbf{X} \in \Omega$ and $\mathbf{x} \in \omega$. The virtual work principle, i.e. the weak form of equilibrium, has the standard form,

$$G_s(\boldsymbol{\varphi}, \delta\boldsymbol{\varphi}; p) = \int_\Omega \mathbf{P} \cdot \operatorname{Grad} \delta\boldsymbol{\varphi} \, \mathrm{d}V - \int_{\Gamma_l} \mathbf{T} \cdot \delta\boldsymbol{\varphi} \, \mathrm{d}S = 0 \qquad \forall \, \delta\boldsymbol{\varphi}, \tag{62}$$

where Γ_l is the lubricated contact surface in the reference configuration and $\mathbf{T}$ is the nominal surface traction resulting from the hydrodynamic interaction on Γ_l, which is here, for simplicity, assumed to be the only loading. The formulation can be extended in the standard manner to include other loads, such as prescribed surface traction, body forces, unilateral contact, etc. The pressure field p has been introduced as an additional argument of the functional G_s to indicate that the solid subproblem is coupled to the fluid subproblem through the dependence of the traction $\mathbf{T}$ on p.

The virtual work principle can be written in an equivalent form with the traction term evaluated in the current configuration and expressed in terms of the spatial surface traction $\mathbf{t}$,

$$G_s(\boldsymbol{\varphi}, \delta\boldsymbol{\varphi}; p) = \int_\Omega \mathbf{P} \cdot \operatorname{Grad} \delta\boldsymbol{\varphi} \, \mathrm{d}V - \int_{\gamma_l} \mathbf{t} \cdot \delta\boldsymbol{\varphi} \, \mathrm{d}s = 0 \qquad \forall \, \delta\boldsymbol{\varphi}, \tag{63}$$

where $\gamma_l = \boldsymbol{\varphi}(\Gamma_l)$ is the lubricated contact surface in the current configuration, and the spatial (Cauchy) traction $\mathbf{t}$ is given by Eq. (46). For a hyperelastic solid, the first Piola–Kirchhoff stress $\mathbf{P}$ is governed by the elastic strain energy function $W(\mathbf{F})$ according to

$$\mathbf{P} = \frac{\partial W}{\partial \mathbf{F}}, \qquad \mathbf{F} = \operatorname{Grad} \boldsymbol{\varphi}, \tag{64}$$

where $\mathbf{F}$ is the deformation gradient.

7.2 *Fluid Part*

As discussed in Sect. 6, the fluid subproblem is governed by the Reynolds equation that is formulated on the lubrication surface $\mathcal{S}$. When one of the physical surfaces is rigid, as assumed here, it is convenient to define the lubrication surface as the projection of the deformed lubricated contact surface γ_l onto the rigid countersurface, thus $\mathcal{S} = \mathcal{P}(\gamma_l)$, where $\mathcal{P}(\mathbf{x})$ denotes the orthogonal projection of point $\mathbf{x} \in \gamma_l$ onto the rigid countersurface, see Fig. 14. It is stressed that the deformed lubricated contact surface $\gamma_l = \boldsymbol{\varphi}(\Gamma_l)$ depends on the solution of the solid subproblem and so does $\mathcal{S}$.

As a special case of the general weak form (49), the weak form of the steady-state Reynolds equation with the Dirichlet boundary condition prescribed on the whole boundary, i.e. $\partial_p \mathcal{S} = \partial \mathcal{S}$, takes the following simple form:

$$G_f(p, \delta p; \boldsymbol{\varphi}) = \int_{\mathcal{S}} \mathbf{q} \cdot \operatorname{grad}_{\mathcal{S}} \delta p \, \mathrm{d}s = 0 \qquad \forall \, \delta p, \tag{65}$$

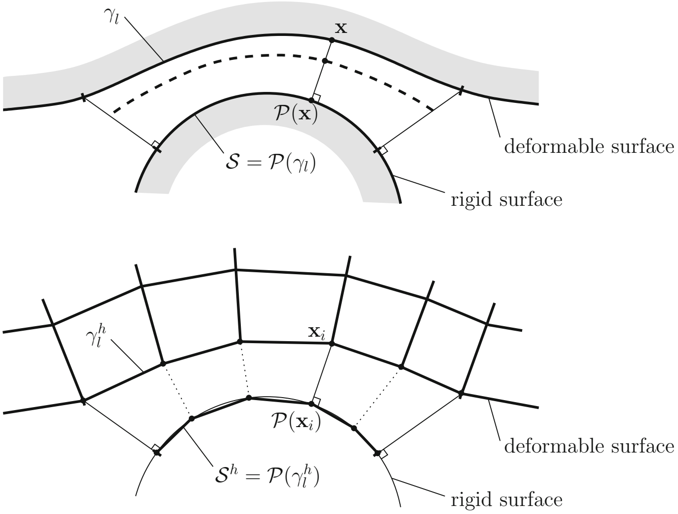

Fig. 14 The solution-dependent lubrication surface $\mathcal{S}$ ($\mathcal{S}^h$) is defined by the projection of the lubricated contact surface γ_l (γ_l^h) onto the rigid countersurface: continuum (*top*) and discretized (*bottom*) setting. The dashed line in the top figure indicates an intermediate surface that could also be adopted as the lubrication surface, see Stupkiewicz et al. (2016) and Temizer and Stupkiewicz (2016)

where $\boldsymbol{\varphi}$ has been introduced as an additional argument of the functional G_f to indicate the respective coupling, e.g., through the film thickness h.

The cavitation is not considered here to make the formulation of the coupled soft-EHL problem possibly simple. In fact, adding the cavitation does not change the general structure of the problem, and it is included in the illustrative examples provided in Sect. 8.

7.3 *Elasto-Hydrodynamic Coupling*

The strong coupling of the two subproblems introduced above constitutes the essential feature of the EHL problems. Specifically:

(i) the lubricant film thickness h, which influences the lubricant flow through the Reynolds equation, depends on the deformation of the solid, cf. Eqs. (36)–(37);
(ii) the load, i.e. the surface traction $\mathbf{t}$ in the virtual work principle (63), depends on the hydrodynamic pressure p and its gradient, cf. Eq. (46);
(iii) the lubrication surface $\mathcal{S}$, on which the Reynolds equation is formulated, depends on the deformation of the solid through the projection $\mathcal{S} = \mathcal{P}(\gamma_l)$.

The first and the second coupling are characteristic for all EHL problems. The third coupling is solely due to the finite-deformation effects, and it is not present in the small-deformation framework that is usually adopted in the EHL theory. Note also that the effect of the shear stresses on the deformation of the solid is usually neglected in the EHL theory, and only the pressure loading is considered. However, in soft-EHL problems, this assumption is not necessarily valid, see Stupkiewicz and Marciniszyn (2009). The couplings listed above have already been symbolically indicated in the weak forms (63) and (65) by including p and $\boldsymbol{\varphi}$ as the arguments of the functionals G_s and G_f, respectively.

7.4 Finite-Element Treatment

Following the standard approach, the finite-element approximation of the unknown fields of placement $\boldsymbol{\varphi}$ and pressure p is introduced,

$$\boldsymbol{\varphi}^h = \sum_i N_i^{(\varphi)} \boldsymbol{\varphi}_i, \qquad p^h = \sum_i N_i^{(p)} p_i, \tag{66}$$

where $\boldsymbol{\varphi}_i = \mathbf{X}_i + \mathbf{u}_i$ denotes the placement of the i-th node, $N_i^{(\varphi)}$ is the corresponding basis function, $\mathbf{X}_i$ is the position of the node in the reference configuration and $\mathbf{u}_i$ is the nodal displacement, which is the actual unknown in the standard finite-element formulation. Similarly, p_i denotes the nodal pressure and $N_i^{(p)}$ the corresponding basis function. Recall that the pressure field is defined on the lubrication surface $\mathcal{S}$ while the displacement is defined in the bulk domain Ω. In the Galerkin method, the test functions are approximated using the same basis functions, thus

$$\delta\boldsymbol{\varphi}^h = \sum_i N_i^{(\varphi)} \delta\boldsymbol{\varphi}_i, \qquad \delta p^h = \sum_i N_i^{(p)} \delta p_i. \tag{67}$$

Discretized weak forms are now obtained by introducing the approximations (66)–(67) into the weak forms (63) and (65), viz.

$$G_s^h(\mathbf{U}, \delta\mathbf{U}; \mathbf{P}) = G_s(\boldsymbol{\varphi}^h, \delta\boldsymbol{\varphi}^h; p^h) = 0 \qquad \forall\, \delta\mathbf{U}, \tag{68}$$

and

$$G_f^h(\mathbf{P}, \delta\mathbf{P}; \mathbf{U}) = G_s(p^h, \delta p^h; \boldsymbol{\varphi}^h) = 0 \qquad \forall\, \delta\mathbf{P}, \tag{69}$$

where $\mathbf{U}$ and $\mathbf{P}$ denote the global vectors of unknown nodal displacements and pressures, respectively. Since G_s^h is linear in $\delta\mathbf{U}$ and G_f^h is linear in $\delta\mathbf{P}$ we have

$$G_s^h(\mathbf{U}, \delta\mathbf{U}; \mathbf{P}) = \mathbf{R}_s(\mathbf{U}; \mathbf{P}) \cdot \delta\mathbf{U}, \quad G_f^h(\mathbf{P}, \delta\mathbf{P}; \mathbf{U}) = \mathbf{R}_f(\mathbf{P}; \mathbf{U}) \cdot \delta\mathbf{P}, \tag{70}$$

so that the problem can be written in the residual form,

$$\mathbf{R}_s(\mathbf{U};\mathbf{P}) = \mathbf{0}, \qquad \mathbf{R}_f(\mathbf{P};\mathbf{U}) = \mathbf{0}, \tag{71}$$

or, with a view to applying a monolithic solution scheme, in the following form,

$$\bar{\mathbf{R}}(\bar{\mathbf{U}}) = \mathbf{0}, \qquad \bar{\mathbf{R}} = \{\mathbf{R}_s, \mathbf{R}_f\}, \qquad \bar{\mathbf{U}} = \{\mathbf{U}, \mathbf{P}\}. \tag{72}$$

In the monolithic scheme, the nonlinear equation (72) is solved simultaneously with respect to all unknowns, and the Newton method is used here for that purpose. The tangent matrix required by the Newton method can be efficiently obtained using the automatic differentiation (AD) technique (Korelc 2009; Korelc and Wriggers 2016). Since Eq. (72) governing the coupled problem is highly nonlinear, convergence of the iterative Newton scheme cannot be guaranteed. This problem can be circumvented by applying a kind of continuation method in which the desired solution is obtained by gradually increasing the load (or by varying another influential parameter) and by using the converged solution as the initial guess for the subsequent solution corresponding to the increased load. This approach proved successful in solving a wide range of fully-coupled finite-deformation soft-EHL problems (e.g., Stupkiewicz and Marciniszyn 2009; Stupkiewicz et al. 2016); selected examples are presented in the next section.

8 Soft-EHL: Illustrative Examples

Three illustrative examples of the soft-EHL problems that involve finite deformations of the solid are briefly described in this section. The examples are taken from our earlier work (Stupkiewicz 2009; Stupkiewicz et al. 2016), where more details can be found.

8.1 Reciprocating O-Ring Seal

In this section, selected results are presented for the reciprocating elastomeric O-ring seal that has been studied in detail by Stupkiewicz (2009), see also Stupkiewicz and Marciniszyn (2009). Due to the simple geometry (circular cross section), the O-ring seal is a suitable benchmark problem, and it is frequently studied in various contexts (e.g., Fatu and Hajjam 2011; Yang and Salant 2011; Shin et al. 2016).

The general geometrical setup of a hydraulic seal is shown in Fig. 15. Due to the action of the sealed pressure, the seal is compressed between the housing and the rod, and this is accompanied by visibly finite deformations, see Fig. 16. The reciprocating motion of the rod results in the buildup of the hydrodynamic pressure at the rod–seal interface, and the analysis below is limited to the steady-state hydrodynamic lubrication during the *outstroke* (the rod moves towards the air side, $U > 0$) and *instroke* (the rod moves towards the sealed pressure side, $U < 0$). The unilateral

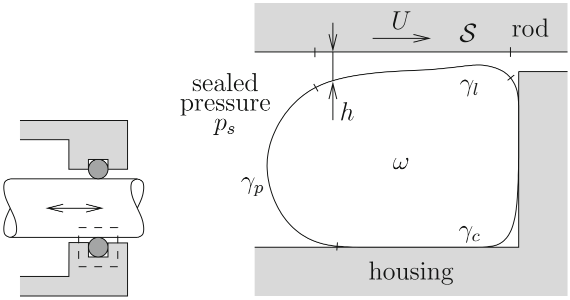

Fig. 15 Reciprocating O-ring seal: schematic of the problem

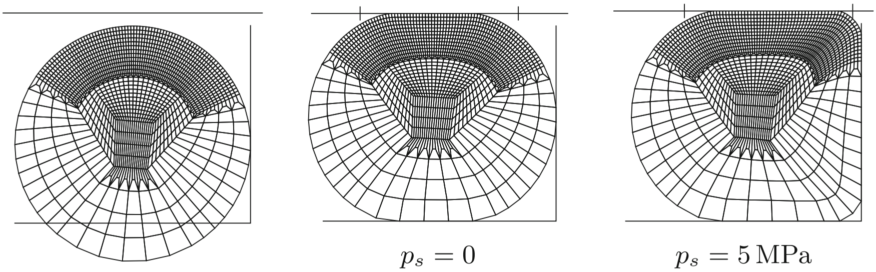

Fig. 16 O-ring seal: finite-element mesh (mesh density 2) in the undeformed configuration (*left*) and in the deformed configuration for two values of the sealed pressure p_s. The housing and the rod are rigid and are represented by solid lines (reproduced from Stupkiewicz 2009)

contact with the housing is also included in the model, and both the rod and the housing are assumed to be rigid. Axial symmetry with respect to the rod axis is assumed so that the problem is two-dimensional, and thus the Reynolds equation becomes one-dimensional.

The seal is assumed to be hyperelastic, governed by the Mooney–Rivlin material model. All the geometrical, material and process parameters can be found in Stupkiewicz (2009). Note that the maximum sealed pressure, $p_s = 5\,\mathrm{MPa}$, exceeds the shear modulus of the seal, $\mu = \mu_1 + \mu_2 = 3.66\,\mathrm{MPa}$. Five mesh densities have been used in the computations with the total number of unknowns ranging from about 1,000 for mesh density 1 to 190,000 for mesh density 16. The mass-conserving cavitation model, cf. Sect. 6.5, is not employed in this example. Instead, the cavitation condition is approximately enforced using the penalty method (Wu 1986).

Figure 17 shows the hydrodynamic pressure and the film thickness for two values of the sealed pressure p_s. It can be seen that a characteristic ridge is formed at outlet, i.e. on the right (left) in the case of the outstroke (instroke). The pressure profiles corresponding to the outstroke and instroke are very similar except for fine details at the inlet and outlet. In particular, a small pressure dimple is observed at the outlet during the instroke, while, at the same location, which corresponds to the inlet during the outstroke, the pressure increases monotonically. A similar dimple is not formed

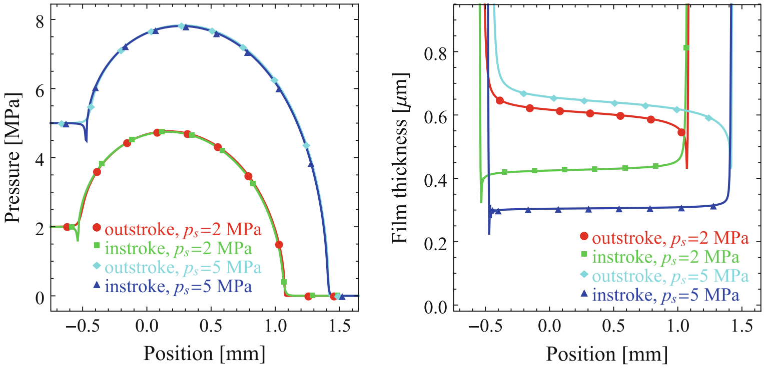

Fig. 17 O-ring seal: the effect of the sealed pressure p_s on the hydrodynamic pressure p (*left*) and film thickness h (*right*) for the rod speed $U = 100$ mm/s (mesh density 16). Position $x = 0$ corresponds to the position of the center of the cross section in the undeformed configuration, see Fig. 16 (reproduced from Stupkiewicz 2009)

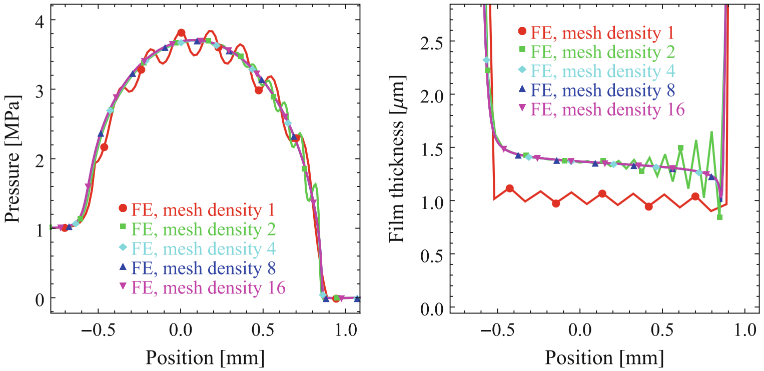

Fig. 18 O-ring seal: convergence with mesh refinement in terms of the pressure p (*left*) and of the film thickness h (*right*) (reproduced from Stupkiewicz 2009)

at the outlet during the outstroke because the pressure would then decrease below zero, which is prevented by the cavitation condition.

As mentioned above, five mesh densities have been used in the computations to check the performance of the computational scheme and convergence with mesh refinement. In particular, it has been observed that spurious oscillations of pressure and film thickness may occur in some situations. This is illustrated in Fig. 18 which shows convergence of the solution with mesh refinement. The oscillations of the film thickness have a zigzag-like appearance which is related to the piecewise-linear finite-element approximation of the displacement field on the boundary. The approximation of the hydrodynamic pressure is here piecewise-polynomial and hence the wavy appearance of the pressure oscillations.

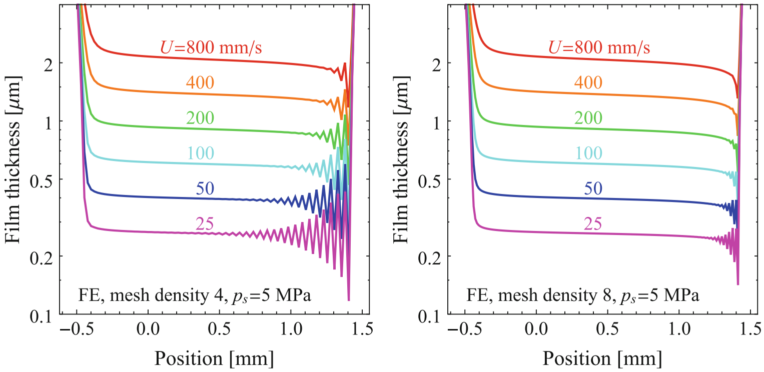

Fig. 19 O-ring seal: effect of the rod speed U and mesh density on the film thickness h for mesh density 4 (*left*) and mesh density 8 (*right*). The more severe lubrication conditions, the finer mesh is needed to avoid spurious oscillations (reproduced from Stupkiewicz 2009)

Different orders of approximation of the pressure have been tested in a quest for a remedy to the spurious oscillations. However, the only remedy found is the mesh refinement, as can be observed in Fig. 18. In the case shown in Fig. 18 (outstroke, $p_s = 1\,\text{MPa}$, $U = 400\,\text{mm/s}$), an oscillation-free solution is obtained for mesh density 4 or higher.

The spurious oscillations are further illustrated in Fig. 19 showing the effect of the rod speed and mesh density. It can be seen that the higher the mesh density, the lower the rod speed at which the oscillations appear. Figure 19 shows the results for mesh densities 4 and 8; further reduction of the oscillations is obtained for mesh density 16, see Fig. 15c in Stupkiewicz (2009). This trend is also visible in the other cases studied.

The general conclusion resulting from the convergence studies is that the spurious oscillations occur in severe lubrication conditions, and the severer the lubrication conditions, the finer mesh is necessary to avoid the oscillations. This applies to the finite-element treatment of the Reynolds equation, as illustrated above, but also to the discontinuous Galerkin method that has also been tested, see Stupkiewicz (2009). The low speed of the rod, which results in a small film thickness, is the main factor that promotes the oscillations. Severe conditions are also associated with higher sealed pressures. Interestingly, a solution with mild oscillations may still provide a reasonable estimation of the actual profile of the pressure and the film thickness once the oscillations are filtered out, see Fig. 18.

8.2 *Rigid Cylider Sliding Against a Coated Layer*

In this example, a rigid cylinder is sliding against a soft layer with a harder thin coating, see Fig. 20. A hyperelastic neo-Hookean model is adopted for both the layer and

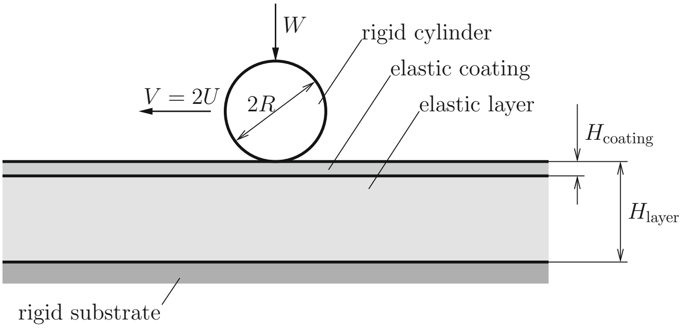

Fig. 20 Rigid cylider sliding against a coated layer (reproduced from Stupkiewicz et al. 2016)

Fig. 21 Coated layer: detail of the deformed finite-element mesh for two values of the load W. A much finer mesh is used in the actual computations (reproduced from Stupkiewicz et al. 2016)

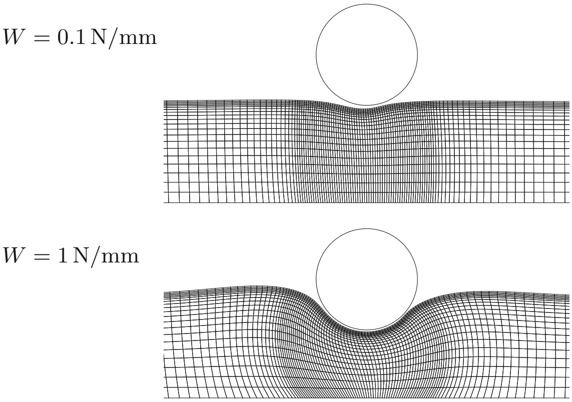

the coating. Steady-state hydrodynamic lubrication is studied in a coordinate system attached to the cylinder. A kind of arbitrary Lagrangian-Eulerian (ALE) description is thus adopted for the layer in which the material flows through the (deformed) finite-element mesh. However, since the layer is elastic, the solid formulation is standard; only the local velocity $\mathbf{v}$ of the material points must be adequately determined in terms of the nominal sliding speed $\mathbf{V}$ according to $\mathbf{v} = \mathbf{F}\mathbf{V}$, where $\mathbf{F}$ is the local deformation gradient. For the material and geometrical parameters used in the computations, the reader is referred to Stupkiewicz et al. (2016).

Figure 21 shows the deformation pattern induced by the lubricated contact. Note that, for better visualization, a coarse mesh is shown in Fig. 21, and a significantly finer mesh has been used in the actual computations. Figure 22 shows the hydrodynamic pressure and the film thickness corresponding to the load W varying between 0.1 and 1 N/mm. To illustrate the effect of finite deformations, which are clearly visible in Fig. 21, the results obtained using the geometrically linear model, i.e. according to the classical EHL theory, are also included in Fig. 22 (indicated by dashed lines). It can be seen that both the pressure and the film thickness are not predicted correctly when the finite-deformation effects are neglected, particularly at the higher loads.

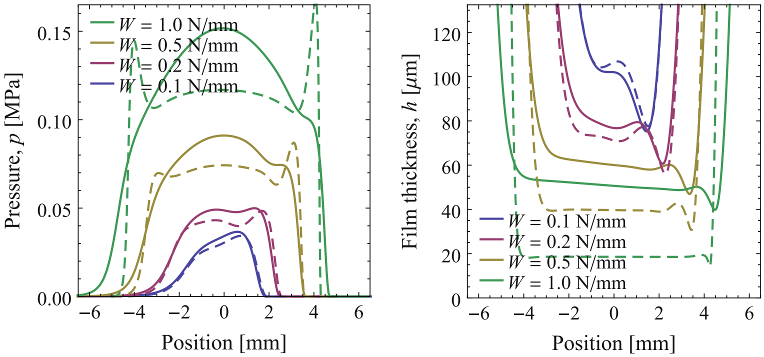

Fig. 22 Coated layer: the hydrodynamic pressure p (*left*) and the film thickness h (*right*) as a function of the load W (nominal entrainment speed $\mu U = 0.1\,\text{N/m}$). Dashed lines indicate the results of the geometrically linear model (reproduced from Stupkiewicz et al. 2016)

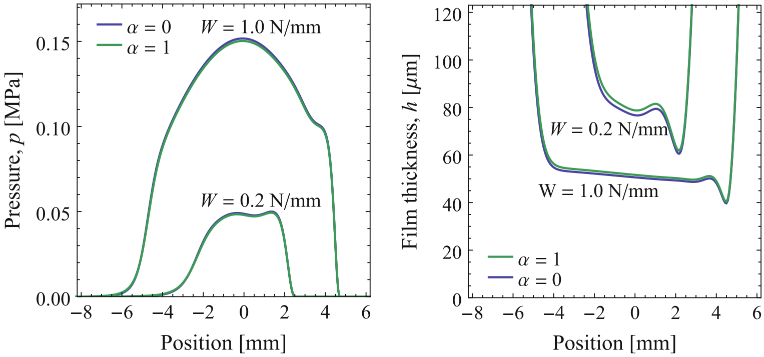

Fig. 23 Coated layer: influence of the position of the lubrication surface $\mathcal{S}$ (specified by parameter α, see text) on the pressure p (*left*) and on the film thickness h (*right*) for $\mu U = 0.1\,\text{N/m}$ (reproduced from Stupkiewicz et al. 2016)

As described in Sect. 7.4, the lubrication surface $\mathcal{S}$ is here defined as the projection on the lubricated contact surface γ_l onto the rigid countersurface, i.e. $\mathcal{S} = \mathcal{P}(\gamma_l)$. Alternatively, surface γ_l itself (i.e. $\mathcal{S} = \gamma_l$) or an intermediate surface (such as that indicated by the dashed line in Fig. 14) could be chosen as the lubrication surface. The effect of this choice is small, as illustrated in Fig. 23. Parameter $\alpha = 0$ corresponds to $\mathcal{S} = \mathcal{P}(\gamma_l)$ and $\alpha = 1$ corresponds to $\mathcal{S} = \gamma_l$. Intermediate values of α are also possible, see Stupkiewicz et al. (2016), but the results are not sensitive to the variation in α, as can already be deduced from Fig. 23.

8.3 *Elastic Ball Sliding Against a Rigid Plane*

In this last example, a hyperelastic ball is slid against a rigid plane in the steady-state hydrodynamic lubrication regime. A constant normal force W is applied at the horizontal mid plane, which is allowed to move vertically as a rigid plane. Further, the symmetry with respect to the vertical mid plane aligned with the sliding direction is exploited so that only one quarter of the ball is included in the model. The setup corresponds to the ball-on-disc test under pure sliding, assuming that the curvature of the sliding path is neglected. The material and geometrical parameters can be found in Stupkiewicz et al. (2016).

The finite-element mesh, shown in Fig. 24, has been refined in the vicinity of the contact zone, with the finest mesh along the trailing edge of the contact zone. Figure 24 shows also the σ_{zz} component of the Cauchy stress in the deformed configuration. At the highest load $W = 40\,\text{N}$, the radius of the contact zone is equal to approximately 50% of the ball radius. The ball is thus deformed in the finite-strain regime, well beyond the Hertzian contact conditions.

Maps of the lubricant film thickness h are shown in Fig. 25 for selected values of the load W and entrainment speed U, the latter defined as one half of the sliding speed V, thus $U = V/2$. The entrainment speed is here provided in the form of the product μU, μ being the fluid viscosity, since the entrainment speed enters the Reynolds equation only through this product. Hence, the effect of increasing the sliding speed (and the entrainment speed) by the factor of two is the same as if the viscosity was increased by the factor of two.

It can be seen in Fig. 25 that a characteristic ridge is formed along the trailing edge of the contact zone. At lower loads and at higher entrainment speeds, the point of the minimum film thickness is located on the symmetry axis, at the rear of the contact zone. Otherwise, there are two minima located at the side lobes. These qualitative features agree well with the results obtained using the classical EHL theory (Hooke 1995).

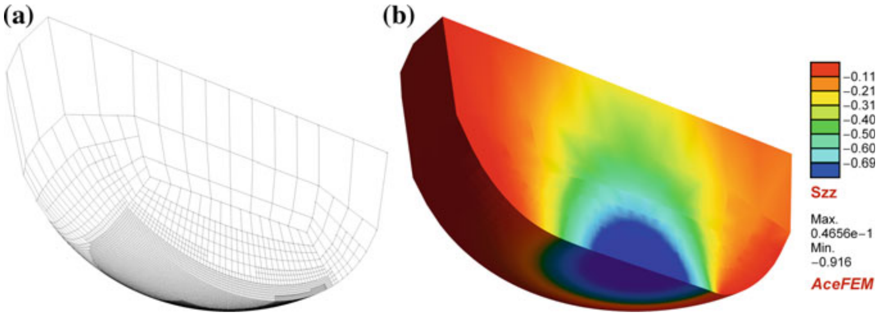

Fig. 24 Elastic ball sliding against a rigid plane: the finite-element mesh (*left*) and the σ_{zz} component of the Cauchy stress (in MPa) in the deformed configuration at the load $W = 40\,\text{N}$ (*right*). The inlet is on the left (reproduced from Stupkiewicz et al. 2016)

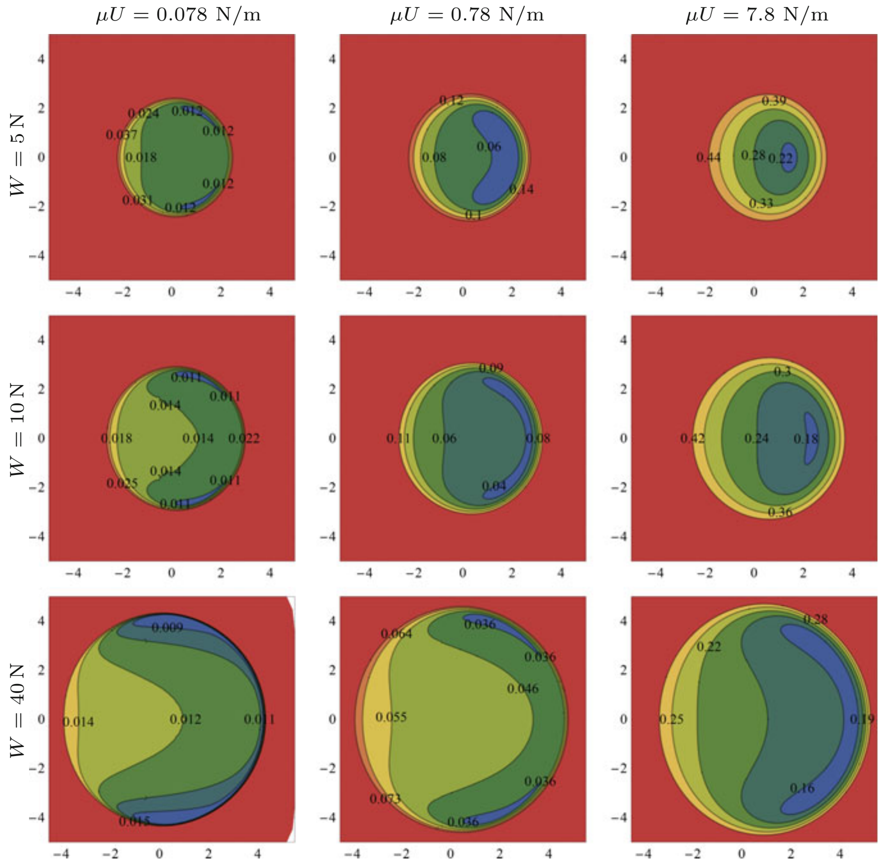

Fig. 25 Elastic ball: maps of the lubricant film thickness h (in mm, position in mm, inlet on the left) (reproduced from Stupkiewicz et al. 2016)

The profiles of the pressure p and the film thickness h along the symmetry axis are shown in Fig. 26. In order to illustrate the finite-deformation effects, the results obtained using the fully nonlinear model (solid lines) are compared to the results obtained using two simplified models. The predictions of the geometrically linear model, in which the configuration changes are neglected as in the classical EHL theory, are denoted by dash-dotted lines. It can be seen that the difference is quite substantial, both in terms of the pressure and the film thickness, for instance, the maximum pressure is 10–15% higher and the minimum film thickness is 10–15% lower in the case of the classical EHL theory. Secondly, the dashed lines depict the results obtained using the geometrically nonlinear model in which the shear (friction) stresses are neglected. It follows that the effect of shear stresses is here negligible. However, as shown by Stupkiewicz et al. (2016), this effect becomes visible, though

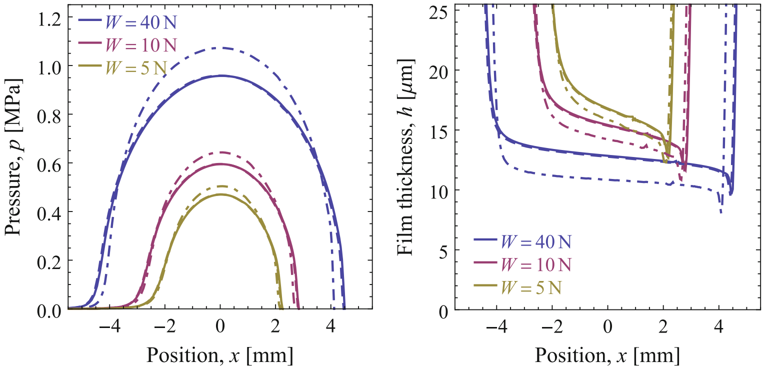

Fig. 26 Elastic ball: pressure p (*left*) and film thickness h (*right*) along the symmetry plane $y = 0$ for $\mu U = 0.078$ N/m. Solid lines denote the nonlinear model, dashed lines denote the nonlinear model without friction stresses, dash-dotted lines denote the geometrically linear model (reproduced from Stupkiewicz et al. 2016)

Fig. 27 Elastic ball: friction coefficient as a function of μU and W. The individual lines correspond to the load W equal to 1, 5, 10, 20 and 40 N (from the top to the bottom) (reproduced from Stupkiewicz et al. 2016)

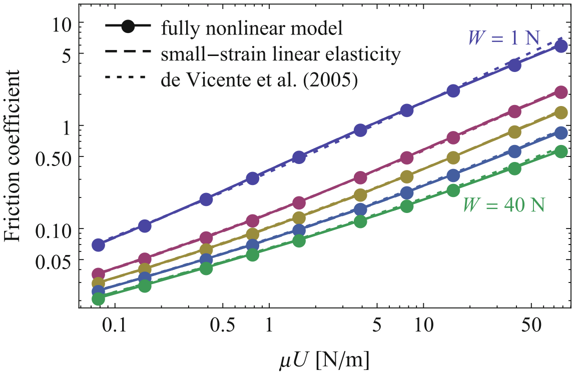

still not substantial, when the entrainment speed μU is increased by one or two orders of magnitude (the respective results are not shown here for brevity).

Interestingly, despite the visible finite deformation effects on the pressure and film thickness, as illustrated in Fig. 26, the friction coefficient is not visibly affected. Figure 27 shows the friction coefficient, defined in the standard manner by dividing the friction force by the normal force, as a function of the entrainment speed μU. It can be seen that the results of the fully nonlinear model and of the geometrically linear model are practically identical while the entrainment speed μU changes by nearly three orders of magnitude and the friction coefficient changes by about two orders of magnitude. The predicted friction coefficient shows also a very good agreement with the regression equation that has been obtained by fitting the predictions of the classical EHL theory (de Vicente et al. 2005).

8.4 Soft-EHL: Summary

In Sects. 6, 7 and 8, we have reviewed the recent progress in the modelling of the soft-EHL problems in the finite-deformation regime. Consistent treatment of the finite-deformation effects in the soft-EHL has several consequences that make the corresponding formulation and its computer implementation distinct from the classical EHL theory.

Finite deformations of one or both contacting bodies may imply finite changes of the lubrication surface, see, e.g., the coated-layer example studied in Sect. 8.2. Accordingly, the Reynolds equation, which is the main tool used for the modelling of the lubricant flow, should be formulated on a non-planar lubrication surface. The corresponding non-classical formulation of the Reynolds equation, provided in Sect. 6, has been here restricted to the case of a time-independent lubrication surface. A detailed discussion of the general case of a time-dependent lubrication surface can be found in Temizer and Stupkiewicz (2016).

At finite deformation, the lubrication surface, as well as its discretization in the computational scheme, depends on the deformation of the solid, and thus it depends on the solution of the EHL problem. This introduces an additional EHL coupling that is not present in the small-strain framework of the classical EHL theory.

Further, an adequate computational method must be used to resolve the finite deformations of the solid. In particular, the elastic half-space approximation, typically used in the classical EHL theory, is not applicable. The finite-element method is here a natural choice, as it provides a general method for treating geometrical and material nonlinearities.

The finite-deformation effects mentioned above are fully accounted for in the computational scheme that is briefly described in Sect. 7.4. So far, the computer implementation is restricted to the case of steady-state problems in which one of the bodies is rigid. Extension to transient lubrication problems for two deformable bodies is a challenging task for future work. The present computational scheme is based on the finite-element method and employs a fully-coupled monolithic solution scheme which proves to perform well.

Representative numerical examples that illustrate the finite-deformation effects have been provided in Sect. 8. Interestingly, in the case of the hyperelastic ball sliding against a rigid plane, the friction coefficient is not affected by the finite deformation of the ball, and the geometrically linear theory delivers accurate predictions of the friction coefficient also at high loads, at which the ball deforms significantly. This result has also been confirmed experimentally, see Fig. 2 in Stupkiewicz et al. (2016).

References

M. J. Adams, B. J. Briscoe, and S. A. Johnson. Friction and lubrication of human skin. *Tribol. Lett.*, 26:239–253, 2007.

P. Alart and A. Curnier. A mixed formulation for frictional contact problems prone to Newton like solution methods. *Comp. Meth. Appl. Mech. Engng.*, 92:353–375, 1991.

A. Almqvist, J. Fabricius, A. Spencer, and P. Wall. Similarities and differences between the flow factor method by Patir and Cheng and homogenization. *Trans. ASME J. Tribol.*, 133:031702, 2011.

T. Almqvist, A. Almqvist, and R. Larsson. A comparison between computational fluid dynamic and Reynolds approaches for simulating transient EHL line contacts. *Tribol. Int.*, 37:61–69, 2004.

J. Andersson, A. Almqvist, and R. Larsson. Numerical simulation of a wear experiment. *Wear*, 271:2947–2952, 2011.

J. F. Archard. Contact and rubbing of flat surfaces. *J. Appl. Phys.*, 24(8):981–988, 1953.

I. I. Argatov. Asymptotic modeling of reciprocating sliding wear with application to local interwire contact. *Wear*, 271:1147–1155, 2011.

G. Bayada and J. B. Faure. A double scale analysis approach of the reynolds roughness comments and application to the journal bearing. *Trans. ASME J. Tribol.*, 111:323–330, 1989.

G. Bayada, I. Ciuperca, and M. Jai. Homogenized elliptic equations and variational inequalities with oscillating parameters. Application to the study of thin flow behavior with rough surfaces. *Nonlinear Anal. Real World Appl.*, 7:950–966, 2006.

H. Ben Dhia and M. Torkhani. Modeling and computation of fretting wear of structures under sharp contact. *Int. J. Num. Meth. Engng.*, 85:61–83, 2011.

B. Bou-Said and M. Kane. Comparison of homogenization and direct techniques for the treatment of roughness in incompressible lubrication. *Trans. ASME J. Tribol.*, 126:733–737, 2004.

A. N. Brooks and T. J. R. Hughes. Streamline upwind/Petrov–Galerkin formulations for convection dominated flows with particular emphasis on the incompressible Navier–Stokes equations. *Comp. Meth. Appl. Mech. Engng.*, 32:199–259, 1982.

G. C. Buscaglia and M. Jai. A new numerical scheme for non uniform homogenization problems: application to the non linear Reynolds compressible equation. *Math. Probl. Engng.*, 7:355–378, 2000.

J. de Vicente, J. R. Stokes, and H. A. Spikes. The frictional properties of Newtonian fluids in rolling–sliding soft-EHL contact. *Tribol. Lett.*, 20:273–286, 2005.

D. Dowson. Elastohydrodynamic and micro-elastohydrodynamic lubrication. *Wear*, 190:125–138, 1995.

D. Dowson and G. R. Higginson. *Elasto-hydrodynamic Lubrication*. Pergamon Press, 1977.

M. Dragon-Louiset. On a predictive macroscopic contact-sliding wear model based on micromechanical considerations. *Int. J. Sol. Struct.*, 38:1625–1639, 2001.

H. G. Elrod. A cavitation algorithm. *Trans. ASME J. Lubr. Technol.*, 103:350–354, 1981.

H. G. Elrod and M. L. Adams. A computer program for cavitation and starvation problems. In D. Dowson, M. Godet, and C. M. Taylor, editors, *Proc. of the First Leeds–Lyon Symposium on Tribology – Cavitation and Related Phenomena in Lubrication*, pages 37–41. Mechanical Engineering, New York, 1974.

P. Farah, W. A. Wall, and A. Popp. An implicit finite wear contact formulation based on dual mortar methods. *Int. J. Num. Meth. Engng.*, 111:325–353, 2017.

A. Fatu and M. Hajjam. Numerical modelling of hydraulic seals by inverse lubrication theory. *Proc. Instn. Mech. Engrs. Part J: J. Engng. Tribol.*, 225:1159–1173, 2011.

S. Fouvry, P. Kapsa, and L. Vincent. Quantification of fretting damage. *Wear*, 200:186–205, 1996.

L. Gallego, B. Fulleringer, S. Deyber, and D. Nelias. Multiscale computation of fretting wear at the blade/disk interface. *Tribol. Int.*, 43:708–718, 2010.

M. Giacopini, M. T. Fowell, D. Dini, and A. Strozzi. A mass-conserving complementarity formulation to study lubricant films in the presence of cavitation. *Trans. ASME J. Tribol.*, 132:041702–1–12, 2010.

A. Hajishafiee, A. Kadiric, S. Ioannides, and D. Dini. A coupled finite- volume CFD solver for two-dimensional elastohydrodynamic lubrication problems with particular application to rolling element bearings. *Tribol. Int.*, 109:258–273, 2017.

M. Hajjam and D. Bonneau. A transient finite element cavitation algorithm with application to radial lip seals. *Tribol. Int.*, 40:1258–1269, 2007.

B. J. Hamrock, S. R. Schmid, and B. O. Jacobsen. *Fundamentals of Fluid Film Lubrication*. Marcel Dekker, New York, 2 edition, 2004.

V. Hegadekatte, N. Huber, and O. Kraft. Modeling and simulation of wear in pin on disc tribometer. *Tribol. Lett.*, 24:51–60, 2006.

C. J. Hooke. The elastohydrodynamic lubrication of elliptical point contacts operating in the isoviscous region. *Proc. Instn. Mech. Engrs. Part J: J. Engng. Tribol.*, 209:225–234, 1995.

B. Jakobsson and L. Floberg. *The finite journal bearing considering vaporization*. Transactions of Chalmers University Technology, vol. 190. Goteborg, Sweden, 1957.

M. Jean. The non-smooth contact dynamics method. *Comp. Meth. Appl. Mech. Engng.*, 177:235–257, 1999.

L. Johansson. Numerical simulation of contact pressure evolution in fretting. *Trans. ASME J. Tribol.*, 116:247–254, 1994.

M. B. Jones, G. R. Fulford, C. P. Please, D. L. S. McElwain, and M. J. Collins. Elastohydrodynamics of the eyelid wiper. *Bull. Math. Biol.*, 70:323–343, 2008.

F. Jourdan and A. Samida. An implicit numerical method for wear modeling applied to a hip joint prosthesis problem. *Comp. Meth. Appl. Mech. Engng.*, 198:2209–2217, 2009.

J. Korelc. Automation of primal and sensitivity analysis of transient coupled problems. *Comp. Mech.*, 44:631–649, 2009.

J. Korelc and P. Wriggers. *Automation of finite element methods*. Springer International Publishing, Switzerland, 2016.

T. A. Laursen. *Computational Contact and Impact Mechanics*. Springer-Verlag, Berlin, 2002.

J. Lengiewicz and S. Stupkiewicz. Continuum framework for finite element modelling of finite wear. *Comp. Meth. Appl. Mech. Engng.*, 205–208:178–188, 2012.

J. Lengiewicz and S. Stupkiewicz. Efficient model of evolution of wear in quasi-steady-state sliding contacts. *Wear*, 303:611–621, 2013.

J. Lengiewicz, J. Korelc, and S. Stupkiewicz. Automation of finite element formulations for large deformation contact problems. *Int. J. Num. Meth. Engng.*, 85:1252–1279, 2011.

J. Lengiewicz, M. Wichrowski, and S. Stupkiewicz. Mixed formulation and finite element treatment of the mass-conserving cavitation model. *Tribol. Int.*, 72:143–155, 2014.

I. R. McColl, J. Ding, and S. B. Leen. Finite element simulation and experimental validation of fretting wear. *Wear*, 256:1114–1127, 2004.

N. Menga and M. Ciavarella. A Winkler solution for the axisymmetric Hertzian contact problem with wear and finite element method comparison. *J. Strain Anal. Eng. Design*, 50:156–162, 2015.

Z. Mróz and S. Stupkiewicz. An anisotropic friction and wear model. *Int. J. Solids Struct.*, 31:1113–1131, 1994.

K. O. Olsson. *Cavitation in dynamically loaded bearings*. Transactions of Chalmers University Technology, vol. 308. Goteborg, Sweden, 1965.

M. Oqvist. Numerical simulations of mild wear using updated geometry with different step size approaches. *Wear*, 249:6–11, 2001.

I. Paczelt and Z. Mróz. On optimal contact shapes generated by wear. *Int. J. Num. Meth. Engng.*, 63:1250–1287, 2005.

N. Patir and H. S. Cheng. An average flow model for determining effects of three-dimensional roughness on partial hydrodynamic lubrication. *Trans. ASME J. Lubr. Technol.*, 100:12–17, 1978.

C. Paulin, S. Fouvry, and C. Meunier. Finite element modelling of fretting wear surface evolution: Application to a Ti–6Al–4V contact. *Wear*, 264:26–36, 2008.

M. Peigney. Simulating wear under cyclic loading by a minimization approach. *Int. J. Sol. Struct.*, 41:6783–6799, 2004.

B. N. J. Persson and M. Scaraggi. On the transition from boundary lubrication to hydrodynamic lubrication in soft contacts. *J. Phys.: Condens. Matter*, 21:185002, 2009.

G. Pietrzak and A. Curnier. Large deformation frictional contact mechanics: continuum formulation and augmented Lagrangian treatment. *Comp. Meth. Appl. Mech. Engng.*, 177:351–381, 1999.

P. Podra and S. Andersson. Simulating sliding wear with finite element method. *Tribol. Int.*, 32:71–81, 1999.

A. Popp, A. Seitz, M. W. Gee, and W. A. Wall. Improved robustness and consistency of 3D contact algorithms based on a dual mortar approach. *Comp. Meth. Appl. Mech. Engng.*, 264:67–80, 2013.

A. Ramalho and J. C. Miranda. The relationship between wear and dissipated energy in sliding systems. *Wear*, 260:361–367, 2006.

O. Reynolds. On the theory of lubrication and its application to Mr. Beauchamp Towers experiments, including an experimental determination of the viscosity of olive oil. *Phil. Trans. R. Soc. Lond. A*, 177:157–234, 1886.

L. Rodriguez-Tembleque, R. Abascal, and M. H. Aliabadi. Anisotropic wear framework for 3D contact and rolling problems. *Comp. Meth. Appl. Mech. Engng.*, 241–244:1–19, 2012.

I. Serre, M. Bonnet, and R. M. Pradeilles-Duval. Modelling an abrasive wear experiment by the boundary element method. *C. R. Acad. Sci. Paris, Serie II b*, 329:803–808, 2001.

G. K. Sfantos and M. H. Aliabadi. Wear simulation using an incremental sliding Boundary Element Method. *Wear*, 260:1119–1128, 2006a.

G. K. Sfantos and M. H. Aliabadi. Application of BEM and optimization technique to wear problems. *Int. J. Sol. Struct.*, 43:3626–3642, 2006b.

D. C. Shin, J. H. Nam, and D. W. Kim. Experimental interior stress fields of a constantly squeezed O-ring modeling from hybrid transmission photoelasticity. *Exp. Mech.*, 40:59–72, 2016.

C. Stolz. A thermodynamical approach to contact wear as application of moving discontiuities. *Arch. Appl. Mech.*, 77:165–175, 2007.

N. Strömberg. An augmented Lagrangian method for fretting problems. *Eur. J. Mech. A/Solids*, 16:573–593, 1997.

S. Stupkiewicz. Finite element treatment of soft elastohydrodynamic lubrication problems in the finite deformation regime. *Comp. Mech.*, 44:605–619, 2009.

S. Stupkiewicz. An ALE formulation for implicit time inegration of quasi-steady-state problems. *Comp. Meth. Appl. Mech. Engng.*, 260:130–142, 2013.

S. Stupkiewicz and A. Marciniszyn. Elastohydrodynamic lubrication and finite configuration changes in reciprocating elastomeric seals. *Tribol. Int.*, 42:615–627, 2009.

S. Stupkiewicz, J. Lengiewicz, and J. Korelc. Sensitivity analysis for frictional contact problems in the augmented Lagrangian formulation. *Comp. Meth. Appl. Mech. Engng.*, 199:2165–2176, 2010.

S. Stupkiewicz, J. Lengiewicz, P. Sadowski, and S. Kucharski. Finite deformation effects in soft elastohydrodynamic lubrication problems. *Tribol. Int.*, 93:511–522, 2016.

I. Temizer and S. Stupkiewicz. Formulation of the Reynolds equation on a time-dependent lubrication surface. *Proc. Roy. Soc. A*, 472:20160032, 2016.

A. Waseem, J. J. Guilleminot, and I. Temizer. Stochastic multiscale analysis in hydrodynamic lubrication. *Int. J. Num. Meth. Engng.*, 112:1070–1093, 2017.

P. Wriggers. *Computational Contact Mechanics*. Springer, Berlin Heidelberg New York, 2nd edition, 2006.

S. R. Wu. A penalty formulation and numerical approximation of the Reynolds-Hertz problem of elastohydrodynamic lubrication. *Int. J. Engng. Sci.*, 24:1001–1013, 1986.

B. Yang and R. F. Salant. Elastohydrodynamic lubrication simulation of O-ring and U-cup hydraulic seals. *Proc. Instn. Mech. Engrs. Part J: J. Engng. Tribol.*, 225:603–610, 2011.

O. C. Zienkiewicz and R. L. Taylor. *The Finite Element Method*. Butterworth-Heinemann, Oxford, 5th edition, 2000.